PROBING THE INFLUENCE OF IMPURITIES ON THE GROWTH OF 2D CADMIUM SELENIDE NANOPLATELETS

by

Ewald Johannes
born in Wiesbaden

Master thesis in chemistry
submitted to Faculty of Chemistry, Pharmaceutical Sciences and Geosciences (FB 09)
of Johannes Gutenberg-University Mainz

5th of April 2019

1. Reviewer: Prof. Dr. Katharina Landfester
2. Reviewer: Prof. Dr. Thomas Basché

Sondieren des Einflusses von Verunreinigung auf das Wachstums von 2D Cadmiumselenid Nanoplättchen

von

Ewald Johannes
geboren in Wiesbaden

1. Gutachter: Prof. Dr. Katharina Landfester
2. Gutachter: Prof. Dr. Thomas Basché

MASTERARBEIT IM STUDIENGANG CHEMIE, BIOMEDIZINISCHE CHEMIE ODER POLYMERCHEMIE
AN DER JOHANNES GUTENBERG – UNIVERSITÄT MAINZ

Ich, Ewald Johannes, Matrikelnummer 2688028 versichere, dass ich meine Masterarbeit selbstständig verfasst und keine anderen als die angegeben schriftlichen und elektronischen Quellen sowie andere Hilfsmittel benutzt habe. Alle Ausführungen, die anderen Schriften wörtlich oder sinngemäß entnommen wurden, habe ich kenntlich gemacht.

Mainz, den 05.04.2019

Ewald Johannes
Johannes Gutenberg-Universität Mainz
Fachbereich Chemie, Pharmazie und Geowissenschaften (FB 09)
Duesbergweg 10-14
55128 Mainz
ejohanne@students.uni-mainz.de

ZUSAMMENFASSUNG

In unserem täglichen Leben begegnen wir meist unbewusst Vorgänge, die auf Energietransfer beruhen. So wird zum Beispiel, von Pflanzen die Energie eines Photons in ein Elektron für die Photosynthese umgewandelt oder in einer Solarzelle aus Licht ein Strom erzeugt. Dafür werden Materialen mit passenden Eigenschaften benötigt. Ein interessantes Beispiel für solche Materialien sind Halbleiternanokristalle. In Abhängigkeit von Größe und Form der Partikel lässt sich deren Bandlücke einstellen.[1] Dies macht sie zu idealen Kandidaten für Anwendungen z.B. in Solarzellen, als absorbierendes Material, und in Lichtquellen (z.B. für Laser oder Displays), als emittierendes Material.[4] In den letzten Jahren wurde eine neue Form von Nanokristallen entdeckt: quasi zweidimensionale Nanoplättchen (NPL). Ihr Hauptvorteil ist eine atomar präzise Dicke in einer Dimension. Es wurden zahlreiche Methoden zur Synthese dieser Partikel entwickelt, ihre Formation ist jedoch noch nicht vollständig verstanden.

Gegenstand dieses Projektes war die Untersuchung eines Phänomens im Wachstum von Cadmiumselenid-Nanoplättchen. Dabei wurde davon ausgegangen, dass dieser Unterschied im Wachstum im Zusammenhang mit einer *a priori* unbekannten Verunreinigung steht. Als erstes wurden die kritische Verunreinigungen in Cadmium-Präkursor durch die Kombination mehrerer analytischer Techniken mit Absorptions- und Photolumineszenz-Spektren, die während des Wachstums aufgenommen wurden, identifiziert. Zur Untersuchung des Einflusses der gefunden Verunreinigungen auf das Wachstum von Cadmiumselenid Nanoplättchen, wurde das System gezielt mit diesen Verunreinigungen in unterschiedlichen Konzentrationen dotiert. Die verschiedenen gefunden Verunreinigungen wirken sich jedoch in unterschiedlicher Weise auf das Wachstum aus. Durch die identifizierte Trifluoressigsäure (TFA nach engl.: *trifluoroacetic acid*) konnte ein ähnliches Ergebnis wie mit dem verunreinigten Cadmium-Vorläufer erzielt werden, nämlich die Bildung einer einzelnen Nanoplättchen-Dicken-Fraktion. Im Vergleich zu verunreinigtem Cadmium-Präkursor waren weitaus höhere Konzentrationen an TFA nötig. Zudem wurden Unterschiede im Reifungsverhalten des Replicas zum Original entdeckt. Die höhere Konzentration an TFA (mehr als das 10-fache) zeigt, dass das Replica die Oberflächenenergie des Systems ändert. Im Fall des Originalsystems hingegen sind die identifizierten Konzentrationen an TFA (3 mol%) sehr gering und ändern das Wachstumsverhalten vermutlich eher über die Senkung der Bildungsenthalpie des Cadmiumselenid Monomers. Diese Ergebnisse harmonisieren mit den neusten Erkenntnissen aus der Literatur.[4],[24]

In weiteren Untersuchungen sollte erforscht werden, ob die Schichtdicke der Plättchen und die Verteilung der Fraktionen mit unterschiedlicher Schichtdicken im finalen Produkt durch die Änderung der Reaktionsparameter (Zugabezeipunkt und Temperaturprogram) variiert werden kann. Die unterschiedlichen Wachstumsverhalten könnten aus strukturellen Differenzen in den Cadmium-Präkusoren stammen. So könnten gemischte Koordinationspolymere aus Cadmiummyristat und -trifluoracetat der Grund sein. Dies könnte mit weiteren ^{113}Cd-ssNMR-Messungen an Cadmiummyristat und -trifluoracetat adressiert werden. Andere Liganden für den Cadmium-Vorläufer sollten auch in Erwägung gezogen werden, wie z.B. mono-, dichlor- oder Cyanessigsäure, da mit diesen die Bindungsstärke zwischen dem Cadmium und der Carbonsäure variiert werden kann. Dies würde wiederum eine zusätzliche, feinere Einstellung der Monomer-Bildungsenthalpie ermöglichen. Dadurch könnten weitere Erkenntnisse über das Wachstumsverhalten von Nanoplättchen gewonnen werden.

CONTENTS

1 INTRODUCTION

Energy transduction plays a key role in our daily life. In nature, plants transduce the energy of a photon to an electron during photosynthesis. In our eyes, photons are transduced to electrochemical potentials. In technology, light is converted into electricity with solar cells and electricity is converted into light with LEDs vice versa. The core of these technologies is the conversion of energy from one form into another. To achieve these conversions materials with tailored properties are needed. Nanomaterials exhibit unique properties, like tunable band-gaps for semiconducting materials. Here, the band-gap depends on the size and shape of the nanomaterial.[1] This feature makes semiconducting nanomaterials a heavily studied material for different energy-related applications. Recently, a novel shape emerged for semiconductor nanocrystals: quasi two-dimensional nanoplatelets (NPL). The major benefit of these materials is their atomically precise thicknesses in one dimension at the ensemble level. Several synthetic routes have been developed for these materials in the past.[2] However, only little is known about their formation mechanisms and even less is understood. Some mechanisms are postulated, like the formation of seeds with the right dimensions, which attach to each other to form platelet seeds that grow from there on,[3] or direct nucleation and growth through a kinetic growth instability.[4] Additives or impurities in the precursors have a strong influence on the growth behavior and the resulting shape.[2]

The growth behavior itself and the influence of impurities could be addressed by absorption and photoluminescence measurement taken during their growth, especially for nanoplatelets due to their characteristic optical feature.[5] Photoluminescence spectroscopy can be used for gathering qualitative information about the appearance of different thickness fractions during growth. Absorption spectroscopy allows for quantitative analyses of appearing and disappearing fractions during growth. Since the precursor's chemical properties and impurity degree influence the reactivity and thus the nucleation and growth of nanoplatelets, detailed analyses of the precursor must be connected with the absorption and photoluminescence data collected during the growth in order to establish correlations. In this project, I investigated a phenomenon in CdSe nanoplatelet growth, which ought to be correlated with an *a priori* unknown impurity. By combining several analytical techniques for the cadmium precursor with absorption and photoluminescence spectra collected during the growth, I identified critical impurities and probed their influence in the growth of CdSe nanoplatelets, followed by intentionally doping the system with these impurities at varying levels. My

results are fitting well with the hypotheses present in the latest literature, which indicates that impurities can either influence growth *via* modification of the surface or by changing the CdSe "monomer" chemical potential. These finding will help to deepen our understanding of these novel class of semiconductor materials.

2 THEORETICAL BACKGROUND

2.1 NANOCRYSTALS

Nanocrystals (NC) are crystallites with sizes between 1 nm and 100 nm. In nanocrystals, the volume to surface ratio changes dramatically compared to bulk materials; it is even possible to have more surface atoms than atoms in bulk. The properties of the used materials alter with their size. In semiconductors, the band gap between valence and conduction band is a materials constant. When the size decreases, the band-gap changes too and gets lager due to quantum confinement effects. For CdSe nanocrystals with sizes smaller than the Bohr radius the band-gap can be shifted across the range of visible light and those nanocrystals are called quantum dots (QD).

a CdSe Bulk Semiconductor

b CdSe Quantum Dot (QD)

1D(e)

1P(e)

Conduction band

1S(e)

E_g(bulk)

E_g(QD)

Valence band

1S(h)
1P(h)
1D(h)

c

$$E_g(\text{QD}) \approx E_{g0} + \frac{\hbar^2 \pi^2}{2 m_{eh} r^2}$$

$$m_{eh} = \frac{m_e m_h}{m_e + m_h}$$

$m_e =$ effective electron mass

$m_h =$ effective hole mass

d

Absorption

QD

Bulk

1D
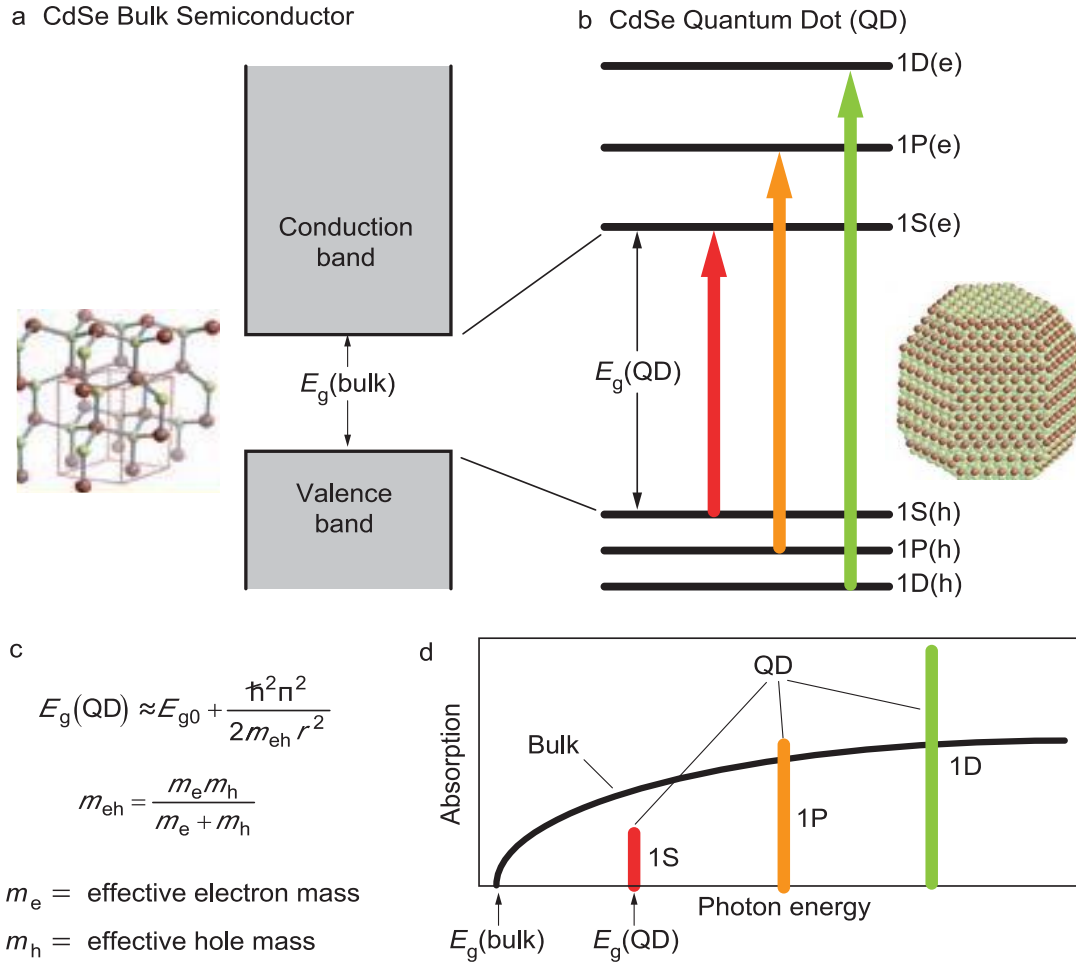
1P

1S

Photon energy

E_g(bulk) E_g(QD)

FIGURE 1: **a** bulk, **b** quantum dot (QD) band diagram, **c** equation for the quantum box, **d** discrete absorption spectra of quantum dot (colored lines) and continuous spectrum for the bulk (black curve).[6]

3

Atoms and molecules have discrete energy states. Bulk semiconductor crystals have an "infinite" number of atoms in all dimensions. These "infinite" number of atoms leads to an "infinite" number of discrete energy states, where their combination results in continuous bands. Semiconductors such as cadmium selenide (CdSe) show a fixed band-gap (E_g(bulk)) that separates the electron-occupied states (the valence band) from the unoccupied states (the conducting band) (figure 1a). When the size decreases, the "infinite" number of atoms and their related states become finite. This means that the band-gap grows and the continuous band transitions into discrete, atomic-like states (figure 1b). Thus, the electronic structure of nanomaterials, below a critical size, is between bulk materials and small molecules. The particle boundaries are "sensed" by electrons and their energy adjusted in response to changes of particle size. This effect is known as the quantum size effect and can be approximated by a "quantum box" model.[7] This is similar to the "particle in a box" model but all three dimensions are regarded and cartesian coordinates are used. The size of the box is related to the QD radius r, so the proportionality is $1/r^2$ (figure 1c). The resulting discrete energies lead to a discrete absorption spectrum for individual QDs (figure 1d, colored bars related to an electronic transition from (b)). Bulk semiconductors have a continuous absorption spectrum, due to their continuous electronic structure (figure 1d, black line).

2.2 GROWTH BY DIFFUSION

Nanocrystals can be synthesized *via* two fundamentally different approaches, either top-down or bottom-up. In the top-down 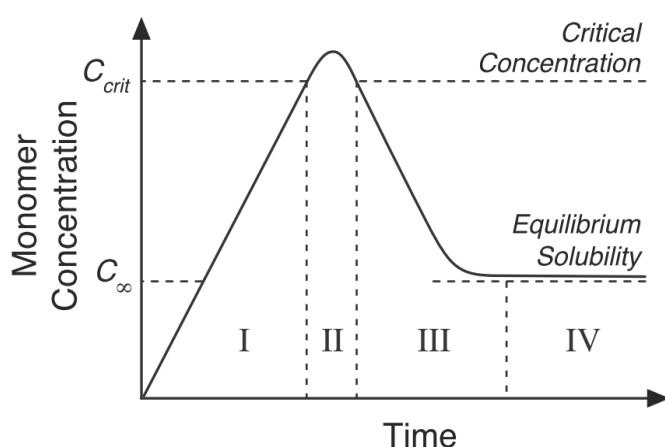approach a big chunk of material is being reduced in its dimension for instance by being grinded, cut or etched *via* versatile methods to obtain nanomaterials. In the bottom-up approach the nanomaterials are formed by nucleation and growth from atoms. For "monodisperse" NC a short nucleation period is followed by growth controlled by diffusion. The growth was observed and described by La-Mer and co-workers for sulfur hydrosols.[8],[9] To understand this phenomenon the temporal evolution of the "monomer

FIGURE 2: LaMer plot of the monomer concentration against time, with critical concentration c_{crit}, equilibriums concentration c_∞ and the four phases.[10]

4

concentration" was followed over the course of a nucleation and growth process (figure 2). The typically observed profile (also known as La-Mer profile) can be split into four stages: I) supersaturation, II) nucleation, III) precursor driven growth and IV) Ostwald-ripening.

In supersaturation stage, the concentration overcomes the saturation c_∞ (the solubility limit) and reaches the critical supersaturation c_{crit}, whereupon the homogeneous nucleation starts.[10] Once the nucleation has started, a decrease in "monomer" concentration occurs, due to the consumption of "monomers" by nuclei formation.

This process can lead to changes in the Gibbs free energy. The sum of the free energy of the bulk ΔG_v and the surface energy γ can be defined as the Gibbs free energy ΔG of a nanoparticle with the radius r (for spherical particles) as described in equation (1). The bulk or crystal energy ΔG_v is dependent on the molar volume V, the Boltzmann constant k_B, the supersaturation S and the temperature T, see equation (2).

$$\Delta G = 4\pi r^2 \gamma + \frac{4}{3}\pi r^3 \Delta G_v \tag{1}$$

$$\Delta G_v = \frac{-k_B T \ln(S)}{V} \tag{2}$$

The bulk free energy ΔG_v is always negative at the conditions at which solid crystals are formed. In contrast the surface free energy γ is positive due to coordinatively unsaturated surface atoms. Therefore, the critical nucleation barrier G_{crit}, can be defined as equation (3). This conditions also determine the critical radius r_c in equation (4).

$$G_{crit} = \frac{4}{3}\pi\gamma r_c^2 \tag{3}$$

$$r_c = \frac{-2\gamma}{\Delta G_v} = \frac{2\gamma V}{k_B T \ln(S)} \tag{4}$$

Before reaching the critical radius r_c, primary particles are formed and dissolve again if they are below the critical radius. Once stable nuclei with sizes larger than the critical
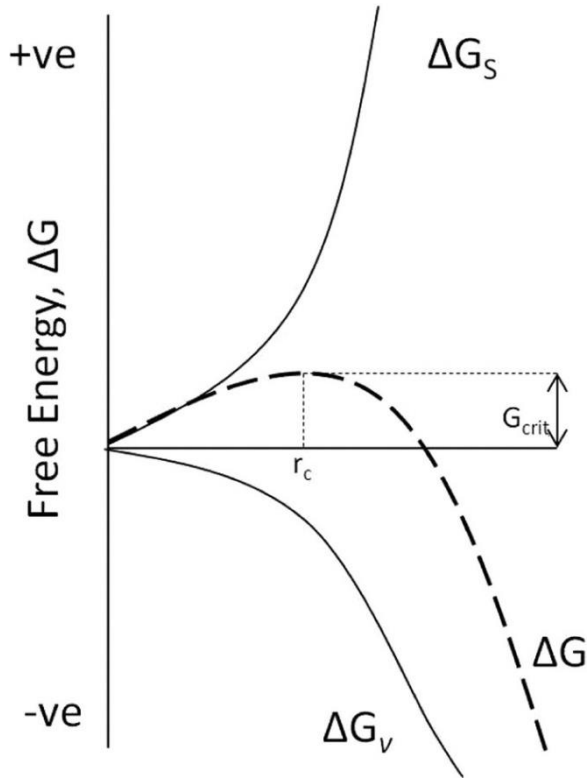
radius are formed they do no longer dissolve but grow by addition of more "monomers". In other words, it exists a critical free energy G_{crit}, as shown in figure 3. Here, the surface free energy ΔG_s, the surface term γ, and the free crystal energy ΔG_v, and the resulting free energy of the particle ΔG are plotted against the particle radius r.[10] Using an Arrhenius type equation (6) a nucleation rate for particles $\frac{dN}{dt}$ can be described with a pre-exponential factor A.

$$\frac{dN}{dt} = A \exp\left(\frac{16\pi\gamma^3 V^2}{3k_B^{\ 3}T^3\,(\ln(S))^3}\right) \qquad (6)$$

FIGURE 3: Free surface energy ΔG_S , volume energy ΔG_V and resulting particles energy ΔG as function of the particles radius r, with critical radius r_c and the corresponding critical energy G_{crit}.[11]

Noteworthy, a chemist has exactly three experimental variables to tune the nucleation of nanocrystals: surface energy γ, temperature T and the supersaturation S. For instance, the surface energy γ can be changed by the choice of the surfactant. All three parameters can be used to influence the nucleation rate $\frac{dN}{dt}$. In an ideal nucleation step in the synthesis of nanocrystals, the nucleation rate should be close to "effectively infinite" as a "burst-nucleation" is desired. After the concentration reaches the level below the critical supersaturation no additional nucleation is occurs.[11]

After the formation of stable nuclei (seeds), we enter the third phase: precursor driven growth. Two mechanisms drive the growth: the monomer diffusion to the surface and the surface attachment reaction. In diluted systems the diffusion is usually the rate-limiting step. Noteworthy, La-Mer's scheme only applies for diffusion limited growth and thus only for diluted systems. After a certain time, the concentration approaches the solubility limit of the smallest nanocrystals. From there on ripening occurs (stage IV), as described by Ostwald already 1900.[12] Here, smaller particles shrink and ultimately even dissolve, and bigger particles grow to the expense of smaller particles. This can be explained by the higher solubility of smaller particles compared to bigger ones

due to their higher surface-to-volume ratio. Therefore, bigger particles are thermody-namically favored, which leads to higher size dispersity of the sample over time.[11]

Even if the synthesis is stopped before QDs undergo Ostwald ripening, they always exhibit a certain size distribution, since in reality the nucleation step is never infinitely fast. Thus, the nucleation occurs over a certain period of time and every nanocrystal in an ensemble starts growing at a different point in time. This means that every nano-crystal in the ensemble has a slightly different size. As the QD size determines their band-gap and thus their emission color, size distribution leads to a distribution of emis-sion colors in the ensemble, leading to a broadened ensemble emission line width.

In first approximation, the accessible shapes for a given crystal system is dictated by the crystal structure of the material. For CdSe two modifications are known, the cubic zinc-blende and the hexagonal wurtzite phases. Under diffusion limited growth condi-tions, the isotropic zinc-blende modification can only form isotropic shapes like cubes and truncated cubes ("spheres"), because the surface reactivity is isotropic in space. For the anisotropic wurtzite modification also anisotropic rod-like shapes are accessible due to the higher reactivity along the crystallographic *c* axis.

2.3 2D MATERIALS

Quasi 2D-semiconducting materials, including CdSe NPLs, exhibit unique beneficial properties. Nanoplatelets are thin rectangular particles, with large lateral dimensions above the Bohr radius. The thickness of a few monolayers (ML) of CdSe units can be atomically precise throughout the ensemble. This leads to distinct optical features for each thickness population. CdSe NPLs of 3, 4 and 5 MLs show their first exciton feature at 462, 515 and 550 nm respectively. Only if the lateral extension is smaller than the Bohr radius, quantum confinement occurs not only across their thickness but also in the lateral dimension. CdSe NPLs exhibit spectral pure fluorescence[13] with a line width around 10 nm[14], enhanced energy transfer rates[15], boosted optical gain[16] and large absorption cross-sections.[17] They are beneficial for a lot of applications like solar cells and light-emitting devices (e.g. lasers and displays).[4] Due to the 1D quantum confine-ment across their thickness the band structure can be considered as a quantum wells. Therefore, NPLs show heavy-hole and light-hole electron transitions, which lead to the characteristic bands in the absorption spectra.[5] Interestingly, the absorption cross sec-tion and thus the extinction coefficient have a non-linear dependence on the surface-area of the NPLs.[17]

Three major theories evolved in the last years that propose possible mechanisms for the formation and growth of CdSe NPLs. Lyashchova *et al.*[18] suggested soft templated

growth. A selenourea-impregnated mesophase of cadmium octanoate with a lamellar structure served as a soft template. A formation by oriented attachment was proposed by Peng *et al.*[3] Peng *et al.* suggested that short and long chain carboxylates are necessary for the formation of NPLs. Seeds (NC with diameter around 2 nm) were used for the growth of 5 ML thick NPLs *via* oriented attachment, where NPLs grow through the addition of cadmium stearate and acetate. The soft-templating growth and necessity of short and long chain carboxylates was ruled out by Riedinger *et al.*[4] With *in situ* X-ray scattering under reaction conditions (above 180 °C) the presence of possible cadmium carboxylate mesophases could not be observed. The necessity of short and long chain carboxylates was ruled out by the direct synthesis of CdSe NPL with either cadmium propionate or cadmium myristate only. Furthermore, a simple model was introduced that considers standard 2D nucleation and growth.[19]

Diffusion is the rate limiting factor for growth in solution, as described in section 2.2. However, at extremely high precursor concentration, similar to a melt, the diffusion rate is much higher compared to the surface reaction rate. In such a scenario the growth is dominated by island nucleation. Noteworthy, all CdSe NPLs protocols published to date use high cadmium concentrations. To fully grow a new layer on an underlying crystal, first a new island has to nucleate on a facet of the underlying crystal. This new island needs to overcome a critical size to become stable, similar to the critical radius in the homogeneous nucleation theory (see section 2.2). When the island exceeds the critical size, it can grow to a full new layer, otherwise it dissolves. For very small crystals with facets below this critical island size, the nucleation barrier is reduced when compared to large facets. This means that on small facets new layers can grow quicker than on large facets. Thus, after a random symmetry breaking event on primary nanocrystals, the small facets grow much faster than the large ones, leading to the formation of NPLs. Hence, this model can explain why and how materials with isotropic crystal structure can grow *via* kinetic instabilities into nanocrystals with anisotropic shapes.

During this process the change of energy of the hole system ΔE is approximated by equation (7), where E_A, E_L and E_V are the energy per area, edge length and volume unit and ΔA, ΔL and ΔV are the respective changes in area, edge length and volume of the growing crystal. The volume energy E_V is always positive and represents the formation energy of the CdSe monomer or the chemical potential μ. The area E_A and edge length energy E_L are always negative and represent the surface and edge energy of the new island.

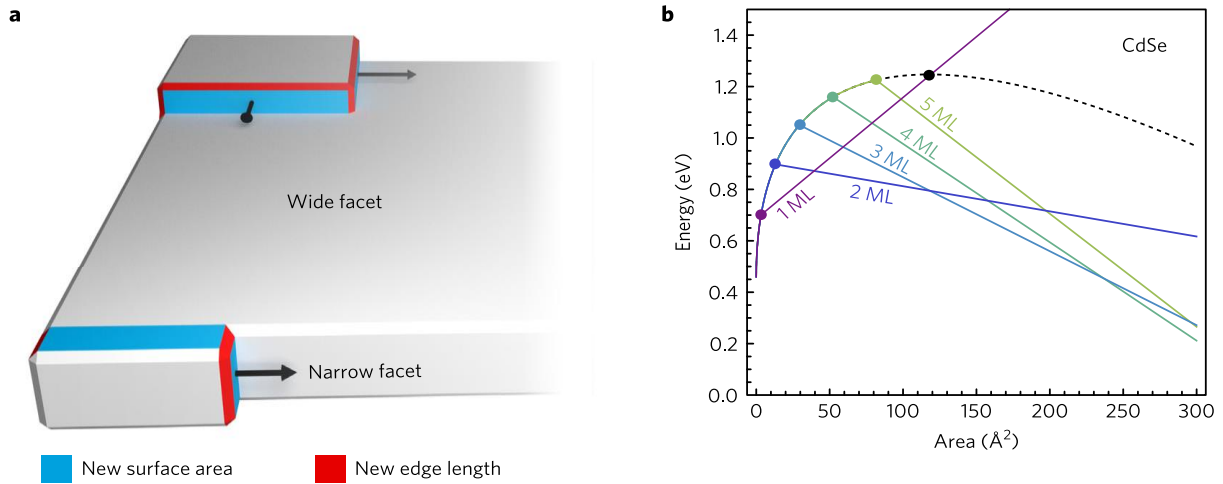$$\Delta E = \Delta V\, E_V + \Delta A\, E_A + \Delta L\, E_L \tag{7}$$

FIGURE 4: **a** illustration of the qualitative difference between growth on narrow and wide facets. **b** island nucleation barrier for wide (black dashed) and narrow (colored) facet against the island size.[4]

In figure 4a, an illustration of the different growth modes on the wide narrow and wide facet is shown, where the new surface area and edge length is highlighted in blue and red. In figure 4b the island energy as function of its size is plotted for CdSe. The energy of the wide facet E^{wide} (black dashed curved) expresses the classic island nucleation. The classical nucleation barrier is the maximum of this curve. The nucleation barriers of narrow facets (colored points) decrease with the number of MLs of the underlying crystal, because during the growth, less edge energy is required to expand the new layer across the facet. Therefore, the island nucleation barrier reduces significantly and thus thin facets grow much faster. However, this mechanism holds true only if the precursor concentration is extremely high and the overall growth rate is limited only by island nucleation and not by diffusion.[4]

Noteworthy, it is also possible to influence the height of nucleation barriers and critical island sizes by the chemical potential (giving rise to E_V) or the surface (E_A and E_L), similar to the classical homogeneous nucleation theory (see section 2.2).

2.4 ADDITIVES

Even small amounts of impurities in the precursors have a dramatic influence on the formation and shape of nanocrystals in synthesis, as it was shown in the past. This knowledge was later used to intentionally add impurities as additives to achieve these special shapes. Traces of phosphonic acid in the solvent trioctylphosphine, for example, lead to rod-shaped nanocrystals and nanowires.[20] The addition of cadmium chloride resulted in CdSe octapods.[21] For lead selenide nanocrystals acetate impurities in the lead oleate precursor promoted the growth of hexagonal stars.[2] The impurities can either influence the surface energy γ or the crystal/bulk energy ΔG_v or E_V respectively. This is not different in nanoplatelet synthesis. Recently it was observed that small amounts of chloride impurities allow for the direct synthesis of six monolayer thick cadmium selenide nanoplatelets.
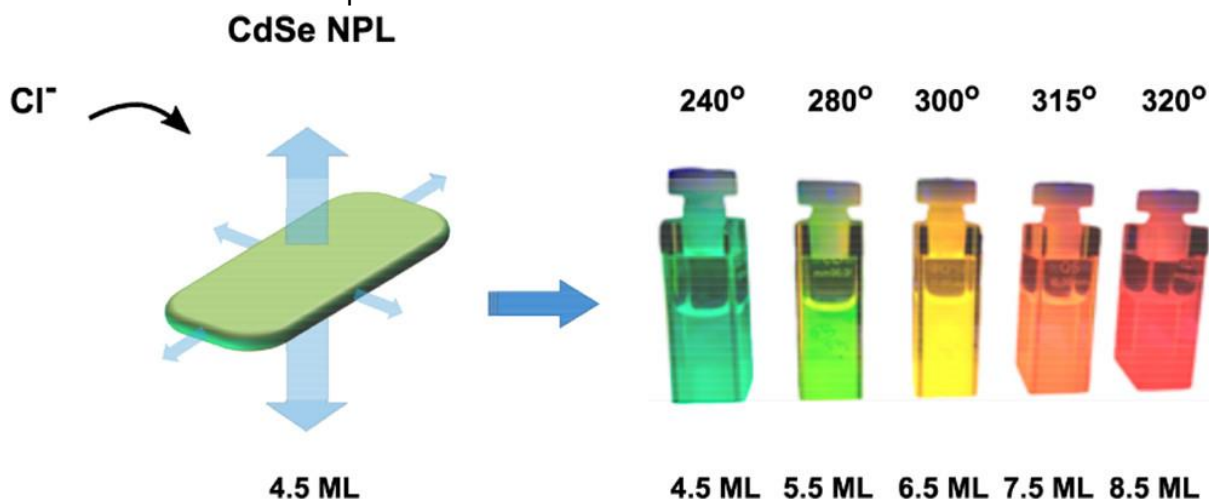
FIGURE 5: Schematically illustration for the influence of chloride on the thickness independence of the temperature and an image of the fluorescent NPL fractions.[22]

This might be explained with the model described by Riedinger *et al.* (see section 2.3). Due to the low amount of chloride (2 mol%), a significant change in surface energy can be ruled out. However, the formation energy of the CdSe monomers can be influenced by the impurities: the formation of CdSe from cadmium acetate and hydrogen selenide show a reaction enthalpy of -94.7 kJ/mol, whereas the formation from cadmium chloride with the same selenium source is endothermic with a reaction enthalpy of 32.9 kJ/mol. A change of only 2 kJ/mol in the reaction enthalpy, equal to 1.6 mol% chloride, would increase the formation energy and changes island nucleation for the wide facet favoring the growth of 6 ML thick NPLs over thinner NPLs.[23]

3 RESULTS AND DISCUSSION

3.1 THE STUDIED PHENOMENON

To synthesize CdSe nanoplatelets, a cadmium precursor is required. A commonly used precursor is cadmium myristate which is usually produced out of cadmium nitrate. The cadmium nitrate is dissolved in methanol and added to a sodium myristate solution, where the cadmium myristate precipitates. Recently, a synthesis of lead oleate was reported by Hendricks *et al.*[24] and modified by Rossinelli *et al.*[25] for cadmium myristate. In this procedure, cadmium oxide is dispersed in acetonitrile and converted into cadmium trifluoroacetate by addition of trifluoroacetic acid and its anhydride. This solution is added to a mixture of triethylamine and myristic acid to allow cadmium myristate to precipitate. Before drying it is washed several times.

It is known, that impurities in the synthesis of CdSe nanoplatelets affect the formation of NPLs strongly (see section 2.4). However, impurities introduced *via* the precursor have not been analyzed so far. By using pure cadmium myristate precursor, independent of the synthetic protocol for the precursor (nitrate method or trifluoroacetate method) and under the same reaction conditions for the synthesis of CdSe NLPs, a mixture of QDs, 3 ML, 4 ML, 5 ML, and a small fraction of 6 ML thick NPLs was obtained. This can be seen in the absorption and photoluminescence spectra (figure 6a). However, in our group we discovered that the use of one specific batch of cadmium myristate (produces by a former lab technician), which is the following will be called "magic" precursor, only yields QDs, and 3 ML and 5 ML thick NPLs (figure 6b).

Hypothetically, impurities from the precursor synthesis could be responsible for the changed growth behavior of NPLs, since all other variables, such as reaction protocol or chemical supplier, were kept the same. The goal of this project was to demonstrate how impurities introduced from the synthesis of cadmium myristate *via* the formation of cadmium trifluoroacetate have an impact on the growth of NPLs. Therefore, several suitable techniques are combined to test this hypothesis.
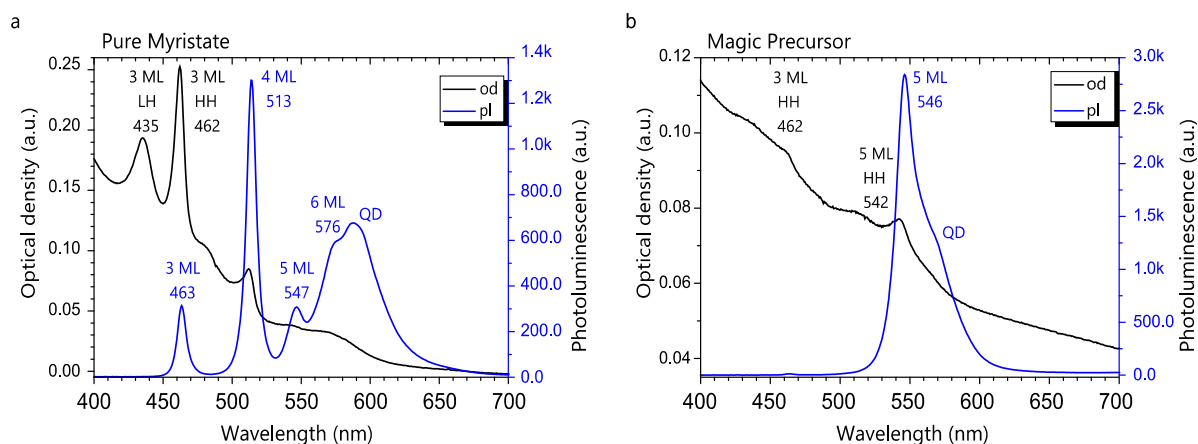
FIGURE 6: Absorption and photoluminescence spectra of the crude reaction solution for synthesis with pure precursor **a** and "magic" precursor **b**.

Before analyzing the "magic" precursor, first a deeper understanding of the growth trajectory is established by *in situ* and *ex situ* absorption and photoluminescence measurements. Afterwards, various analytical methods were used to identify and quantify potential present impurities. Finally, I tested the influence of identified impurities by intentionally adding them to the synthesis and probing their influence by absorption and photoluminescence spectroscopy.

3.2 PROBING THE GROWTH *IN SITU*

To get insight into the growth dynamics, *in* situ photoluminescence and absorption spectroscopy using a dip probe was applied. For better understanding, the synthetic protocol in the following it is shortly described along the temperature program with its critical points as shown in figure 7. First, cadmium myristate and selenium powder are dispersed in 1-octadecene and the solution is degassed and heated to 110 °C. After five minutes at 110 °C the solution is ventilated with argon (figure 7, green cross) and the mixture is again heated up over the course of 16 min to 240 °C. When reaching 180 °C the solution turns yellow, which indicates the formation of a reactive selenium-octadecane species.[26] From there on, the formation

FIGURE 7: Temperature program used for the synthesis, marked the ventilation point by a green cross and the cadmium acetate addition by red bars.

12

of QDs is possible. To promote NPL formation, cadmium acetate is added at 188 °C or 200 °C (figure 7, red marks). In chapter 3.1 and 3.2, the addition temperature is 188 °C and for chapter 3.3 it is 200 °C.. The addition of cadmium acetate leads to a mixed $Cd(myristate)_{2-x}(acetate)_x$ coordination polymer and locally enhances cadmium concentration. The reaction is then held on a reaction temperature of 240 °C for 8 min before the reaction is quenched by rapid cooling to room temperature. The addition temperature and reaction temperature are used to focus the growth on a certain NPL population.

For *in situ* spectroscopy, the three-neck round bottom flask for the synthesis of CdSe NPLs was equipped with an additional neck with a screw cap to place the dip probes into the reaction mixture. For the full coverage of the dip probes in solution, the reactions needed to be upscaled. Thus, the used volume for photoluminescence measurements was two times higher than the volume in usual protocol and for the absorption measurements four times higher.

3.2.1 PHOTOLUMINESCENCE MEASUREMENTS *IN SITU*

For the photoluminescence dip probe, the integration time of the detector is the limiting factor in terms of speed for consecutive measurements or temporal resolution. With our setup it is possible to achieve spectra with good signal-to-noise ratios with an integration time as low as 100 ms, so ten spectra per second can be measured. The measurement was started when reaching the reaction temperature of 150 °C, while heating to 240 °C, and was stopped 3 min after the end of the synthesis in the cooling down step. That means during the synthesis approximately 25 000 spectra were recorded. One major problem for in situ measurements in the course of the synthesis is the thermal quenching of luminescence at higher temperatures. This problem was reported in literature, it was reported for a lot of different II-VI semiconductor QDs[27] [28] or even CdTe NPLs,[29] and also observed during this study. Nevertheless, it is still possible to extract some information from the *in situ* spectra (figure 8). In figure 8a, the *in situ* evolution of photoluminescence is shown from reaching 185 °C ($t = 200$ s) until two minutes before the temperature program is finished ($t = 600$ s). The sharp signal at 611 nm after 300 s (red line) stems from the hood light, which indicates the opening of the flask for cadmium acetate addition. Before addition, a QD fraction appeared at 505 nm and shifted to 615 nm over time. The appearance of a shoulder around 540 nm can be observed while the signal of the QD fraction redshifts.

In figure 8b, the evolution of photoluminescence is shown for the cooling down from 240 °C to 85 °C. An increase in intensity and a blueshift for all peaks can be observed. The shoulder in the spectra at 540 nm shifts to 518 nm when cooling down (grey arrow

in figure 8b). The wavelength of the maximum after cooling indicates that this is the 4 ML thick NPL fraction. A blue shift of 23 nm for the photoluminescence maxima while the temperature is decreased about 155 °C can be seen. For CdTe NPLs a shift of 25 nm is observed with a temperature change of 175 °C.[29]
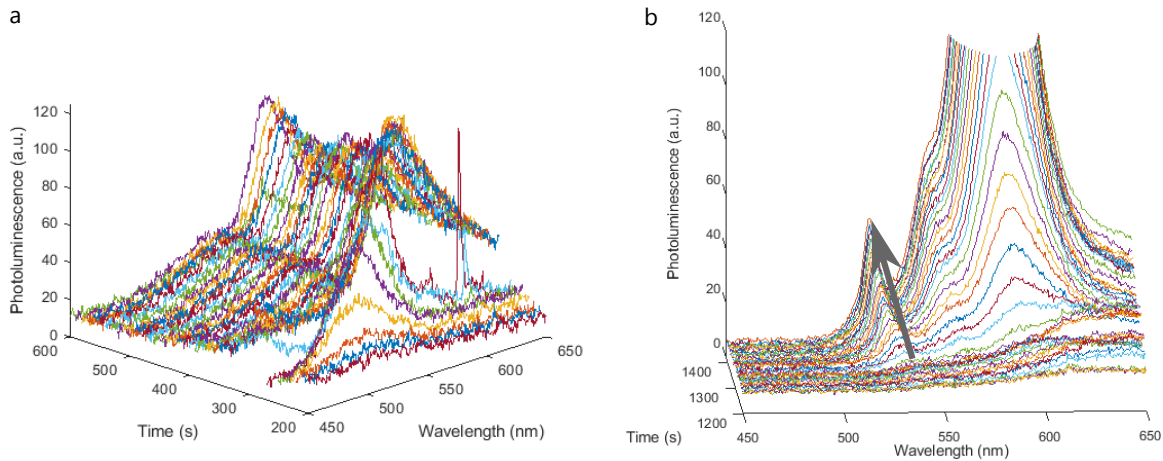

FIGURE 8: Evolution of *in situ* photoluminescence spectra recorded with the dip probe, left side from 185 °C to 240 °C and two min before finished temperature program. Right side cooling down from 240 °C to 85 °C, a gray arrow shows shift direction while cooling down.

The time resolution might be further enhanced and in principle, the setup works well, but it is not suitable for the material studied in this work due to the low high-temperature photoluminescence. Further complications might arise from energy transfer between different NPL fractions and quantum dots. Additionally, the different NPL thickness fractions exhibit different quantum yields. Usually thinner NPLs have lower quantum yields than thicker NPLs. The combination of the above described phenomena leads to a reduced observable luminescence of the thinner NPL fractions up to the complete disappearance of the signal. This limits the information that can be extracted from the *in situ* collected spectra.

3.2.2 ABSORPTION MEASUREMENTS *IN SITU*

During the use of the absorption dip probe, one problem occurred which hindered the successful implementation of the dip probe for *in situ* absorption measurements. One problem is the scattering of the light from gas bubbles accumulated in front of the lens on the dip probe, caused by a small rim between the steel body and the lens. Thereby, a lot of spectra had to be sorted out and a lot of information over long time periods was lost. Some of the obtained spectra are plotted in figure 9. The appearance and shifting of the QD fraction can be observed over time by the appearance and shifting

of the shoulder around 570 nm. Enhancing scattering can be seen by the raising extinction onset at 750 nm over time. Interestingly, no characteristic signals for CdSe NPLs were observed, presumably due to extensive thermal broadening.
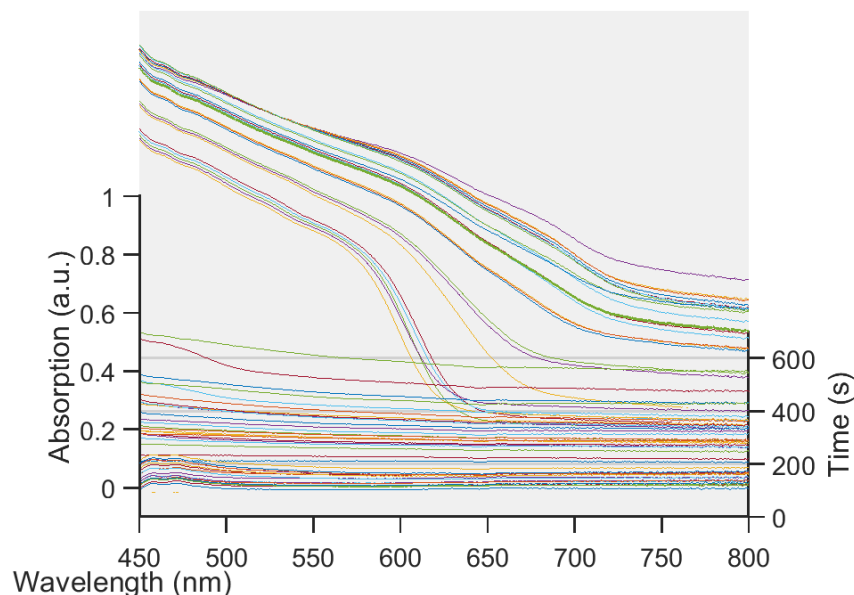
FIGURE 9: Temporal evolution of *in situ* absorption spectra recorded with the dip probe from 150 °C until finished reaction.

Thus, unfortunately the use of the dip probes is not straight forward and even more time to implement improved protocols might not be enough to compensate fundamental limits such as thermal broadening. To gain more insight into the growth dynamics nonetheless, aliquots were taken during the reaction and analyzed *ex situ*. While this method circumvents the thermal broadening issue, the time resolution is substantially reduced and events happening on a very smaller time scale cannot be resolved. However, the time resolution is still sufficient to observe the major trends in the growth dynamics occurring during the reaction.

3.2.3 ALIQUOTS

Aliquots are taken every 30 seconds after the cadmium acetate addition and one aliquot 30 seconds prior to the addition. To prevent the gelation of aliquots while cooling down (which leads to scattering) oleic acid was added to the aliquot dispersions. Oleic acid helps to keep nanomaterials in dispersion and breaks down cadmium coordination polymers over time. However, oleic acid can also dissolve CdSe NPLs similar to what has been reported for alkyl amines.[30] Therefore, samples were measured within 24

15

hours and the dissolution could be avoided. In the following, the results for the synthesis with pure cadmium myristate precursor and for the synthesis with the "magic" precursor are discussed. In both cases, the addition temperature for the cadmium acetate was 188 °C.

For all experiments shown in this work, every second absorption and photoluminescence spectra are shown in the graphs along with the aliquot taken prior to the cadmium acetate addition. All spectra are labeled with the time in relation to the cadmium acetate addition.

3.2.3.1 ALIQUOTS OF A SYNTHESIS WITH PURE CADMIUM MYRISTATE

In the following, the growth of CdSe NPLs synthesized using the pure cadmium myristate precursor is observed for a better understanding of the fundamental growth dynamics of CdSe NPLs.
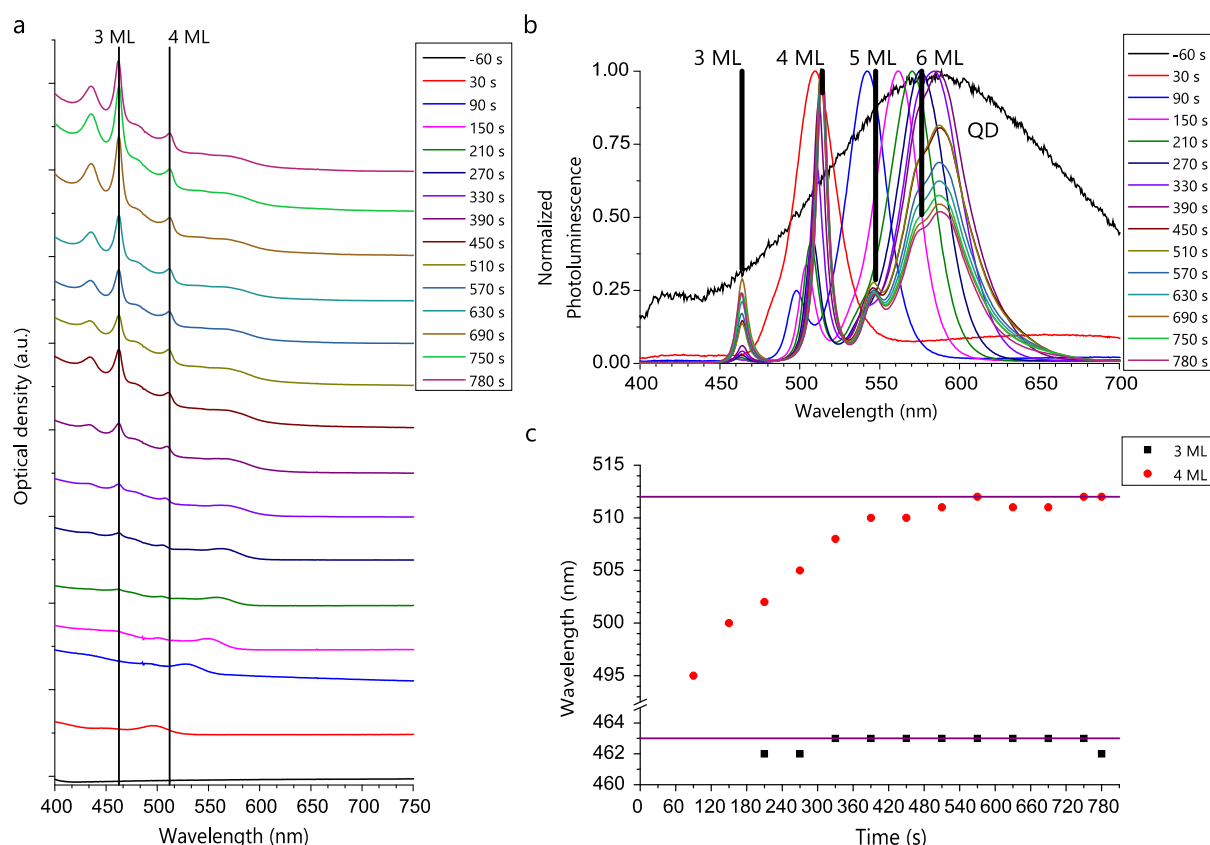
FIGURE 10: **a** Temporal evolution of absorption spectra for synthesis with pure myristate, vertical black lines indicate 3 ML and 4 ML absorption maxima. **b** Temporal evolution of photoluminescence spectra, yellow lines indicate the luminescence maxima for QD, 3, 4, 5 and 6 ML nanoplatelet fraction. **c** Temporal evolution of the observed absorption maxima for 3 ML and 4 ML thick nanoplatelets, with a horizontal purple line for the maximum wavelength of the respective fraction.

16

In the absorption spectra shown in figure 10a, a shoulder at 494 nm appears 30 s after Cd(OAc)$_2$ addition and shifts to 567 nm over the course of the reaction. After 270 s, signals at 462 nm and 505 nm appear and both signals redshift over time to 463 nm and 512 nm respective. Both signals show a broader shoulder at lower wavelengths. This absorption profile is characteristic for CdSe NPLs due to their heavy and light hole transitions, where the broader, blue shifted signal is the light-hole transition and the more intense and narrow signal is the heavy-hole transition.[5] The heavy hole transition wavelengths of 463 nm and 512 nm are characteristic for 3 ML and 4 ML thick NPLs. In the photoluminescence spectra shown in figure 10b, 60 s prior to the Cd(OAc)$_2$ addition, a weak signal around 415 nm is observed together with a broad emission centered at 590 nm. This signal corresponds to small QDs with band edge emission at 415 nm and trap state emission centered around 590 nm. The trap emission can be explained by the tremendous surface-to-volume ratio for the smallest particles. Surface atoms induce trap states in the band-gap of the QDs, a red shifted emission occurs. After the Cd(OAc)$_2$ addition a signal with a maximum at 509 nm is visible and shifts to 588 nm over time, representing the QD fraction. 90 s after Cd(OAc)$_2$ addition, a signal at 450 nm and 497 nm can be observed, which shifts later to 463 nm and 514 nm, characteristic for 3 ML and 4 ML CdSe NPLs. After 330 s, a shoulder around 540 nm appears and shifts to 546 nm, which indicates a growing 5 ML CdSe NPL fraction. At 390 s, the main peak seems to be artificially broadened, and 30 s later a clear shoulder at 573 nm is observed that shifts to 576 nm indicating 6 ML thick CdSe NPLs.

From these observations, the growth of CdSe NPLs can be described as following: After the Cd(OAc)$_2$ addition, the local cadmium concentration is high (within the mixed Cd(myristate)$_{2-x}$(acetate)$_2$ coordination polymer) and the growth of QDs is accelerated while NPL fractions get split off due to kinetic instability, described in section 2.3, as observed in this synthesis for 4, 5 and 6 ML CdSe NPLs by the appearance of shoulders which form a separated, non-shifting fraction. Thus, it can be concluded that NPLs need seeds with the right dimension in the range of the corresponding NPL fraction thickness. After enhancing the cadmium concentration, by Cd(OAc)$_2$ addition the lateral growth of this seeds is promoted and the kinetically favored product is formed, the CdSe NPLs.

3.2.3.2 ALIQUOTS OF A SYNTHESIS WITH "MAGIC" CADMIUM MYRISTATE

The same reaction protocol was applied for the "magic" precursor. In the absorption and photoluminescence spectra are shown in figure 11, and the red-shifting peak assigned to the appearing QD fraction is observed again. However, no peak related to the 4 ML fraction appeared in the absorption (figure 10a). In the photoluminescence

spectra (figure 11b), only a very weak 4 ML CdSe NPLs signal is visible. Instead, a clear absorption of a 5 ML fraction is visible.
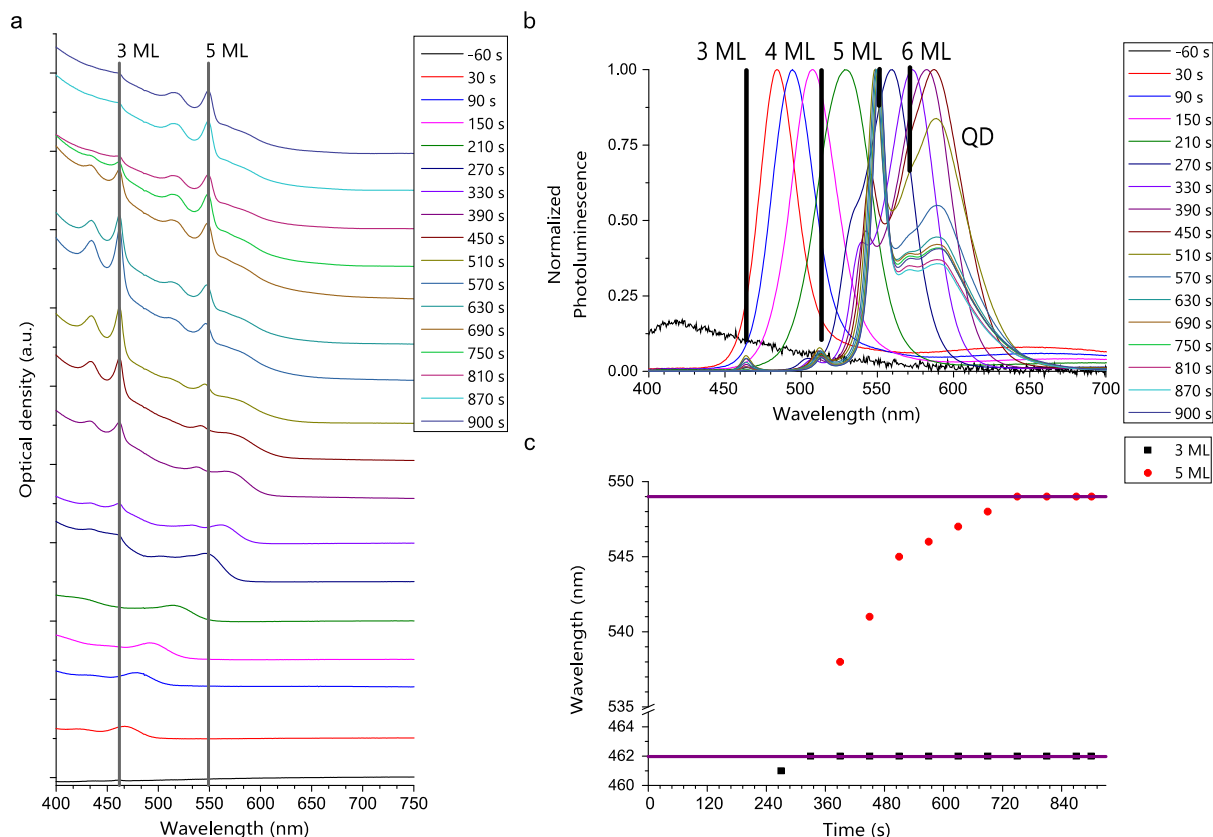

FIGURE 11: **a** Temporal evolution of absorption spectra for synthesis with "magic" precursor, vertical black lines indicate 3 ML and 5 ML absorption maxima. **b** Temporal evolution of photoluminescence spectra, black lines indicate the luminescence maxima for QD, 3, 4, 5 and 6 ML nanoplatelet fraction. **c** Temporal evolution of the observed absorption maxima for 3 ML and 5 ML thick nanoplatelets, with a horizontal purple line for the maximum wavelength of the respective fraction.

Furthermore, it seems that the absorption of the 3 ML fraction is intense in the beginning and decays over time, whereas the absorption of the 5 ML fraction increases over time. This might indicate ripening of the NPLs under the reaction conditions. For CdSe NPL, this already could be observed over long time periods[31] as well as for so-called magic sized clusters.[32] Considering the absorption maxima for the different fractions, during the course of the reaction a redshift for 3 ML and 5 ML NPL spectral features can be observed. However, the maximum of the 3 ML fraction does not shift the opposite way towards shorter wavelengths while the absorption decreases. Similarly, for the magic sized clusters, no blue shift of the absorption for dissolving fractions can be observed.[32]

With these experimental data to hand I can conclude that the different precursors yield different distributions of NPL thickness populations. More precisely, when using the

"magic"-precursor, only 3 and 5 ML thick NPLs can be observed and no 4 ML thick NPL fraction. For the normal precursor, 4 ML thick NPLs are the most abundant thickness population. The question that arises is what changes the growth behavior so drastically that the typically dominant 4 ML fraction no longer appears in absorption spectra when using the "magic"-precursor.

3.3 IMPURITIES OF THE "MAGIC" PRECURSOR AND THEIR IMPACT ON NANOPLATELET SYNTHESES

3.3.1 CHARACTERIZATION OF THE "MAGIC" PRECURSOR

In the first section it could be shown, that different precursors lead to a difference in the formation of CdSe NPLs even though nominally both were cadmium myristate. I hypothesized that impurities in the precursors induce the observed effects. In the following section, the precursors were analyzed by differential scanning calorimetry (DSC), infrared spectroscopy (IR), liquid and solid-state nuclear magnetic resonance spectroscopy (NMR), thermogravimetric analysis (TGA) and x-ray photon spectroscopy (XPS) to quantify and unravel the nature of impurities.

The chemical equations of the precursor synthesis according to Rossinelli *et al.*[25] are as follows:
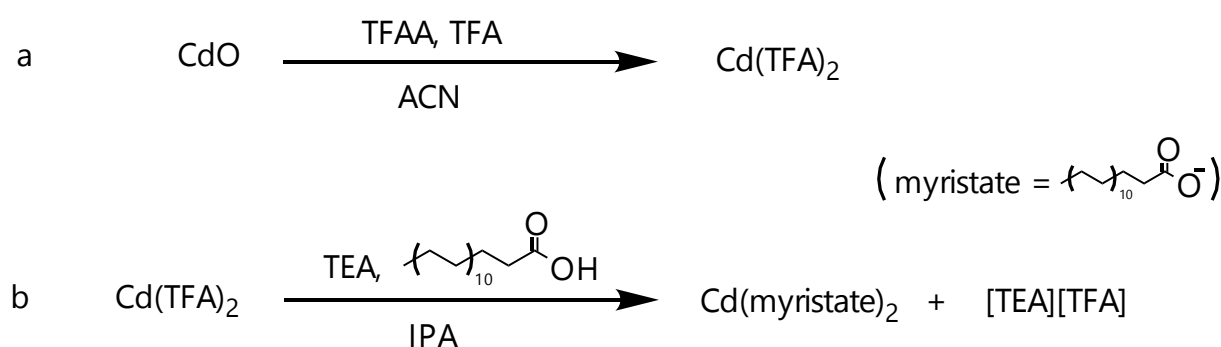
SCHEME 1: Chemical equations for the precursor synthesis *via* cadmium trifluoroacetate, **a** first step, cadmium oxide to cadmium trifluoroacetate; **b** second step, cadmium trifluoroacetate to cadmium myristate.

From the first reaction step (a) acetonitrile (ACN), trifluoroacetic acid (TFA) and its anhydride (TFAA) as both cadmium species, the cadmium oxide (CdO) and the trifluoroacetate ($Cd(TFA)_2$) are possible impurities for the final product $Cd(myristate)_2$. From the second reaction step (b) triethylamine (TEA), isopropanol (IPA), myristic acid and the adduct of triethylamine and trifluoroacetic acid ([TEA][TFA]) could be carried as impurity over into the final product. The solvents, ACN and IPA, are less likely to remain in the product, due to their weak coordinating capability to the cadmium and because they are removed during the purification of precursor in a drying step at 40 °C at reduced pressure over prolonged time. The trifluoroacetic acid anhydride can also be ruled out, because it quickly hydrolyses and forms trifluoracetic acid. Here, water is a possible impurity, due to the hydroscopic nature of TFA.

3.3.1.1 X-Ray Photon Spectroscopy

X-ray photon spectroscopy (XPS) was used for determination of the elemental composition of the cadmium precursor and to identify different elemental species. The samples can be measured without further modification under ultra-high vacuum (UHV). My non-conducting sample were placed on a conducting background for the measurement. Generally speaking, XPS has a penetration depth of 10 nm. Thus, it should be sufficient to analyze the samples because a homogeneous composition within that probed volume can be safely assumed.

For organic compounds, sample decomposition trough x-ray radiation can be a critical issue, as already described by Marshbanks *et al.*[33] for cadmium stearate monolayers. The pure and the "magic" precursor as well as $Cd(TFA)_2$ are investigated by XPS. The color of all samples changed from colorless before the measurement to brown after the measurement. This might be attributed to radiation-induced decomposition of the cadmium myristate and formation of cadmium oxide.

For analysis of all samples, first wide energy range spectra (figure 12a) was recorded and used for qualitative analysis of the constituent elements. All spectra were calibrated to the binding energy of aliphatic carbon atoms at 284.4 eV. Cadmium, carbon and oxygen could be confirmed in all samples. Fluorine could be identified in $Cd(TFA)_2$ as well as in the "magic" precursor. Chloride, like reported in literature[23], could not be identified. The corresponding peaks are marked in figure 12a. The confirmation of fluorine in the "magic" precursor indicates that either $Cd(TFA)_2$ is present as a separated phase in the "magic" precursor or that TFA is present in the form of mixed coordination polymers of the type $Cd(myristate)_{2-x}(TFA)_x$.
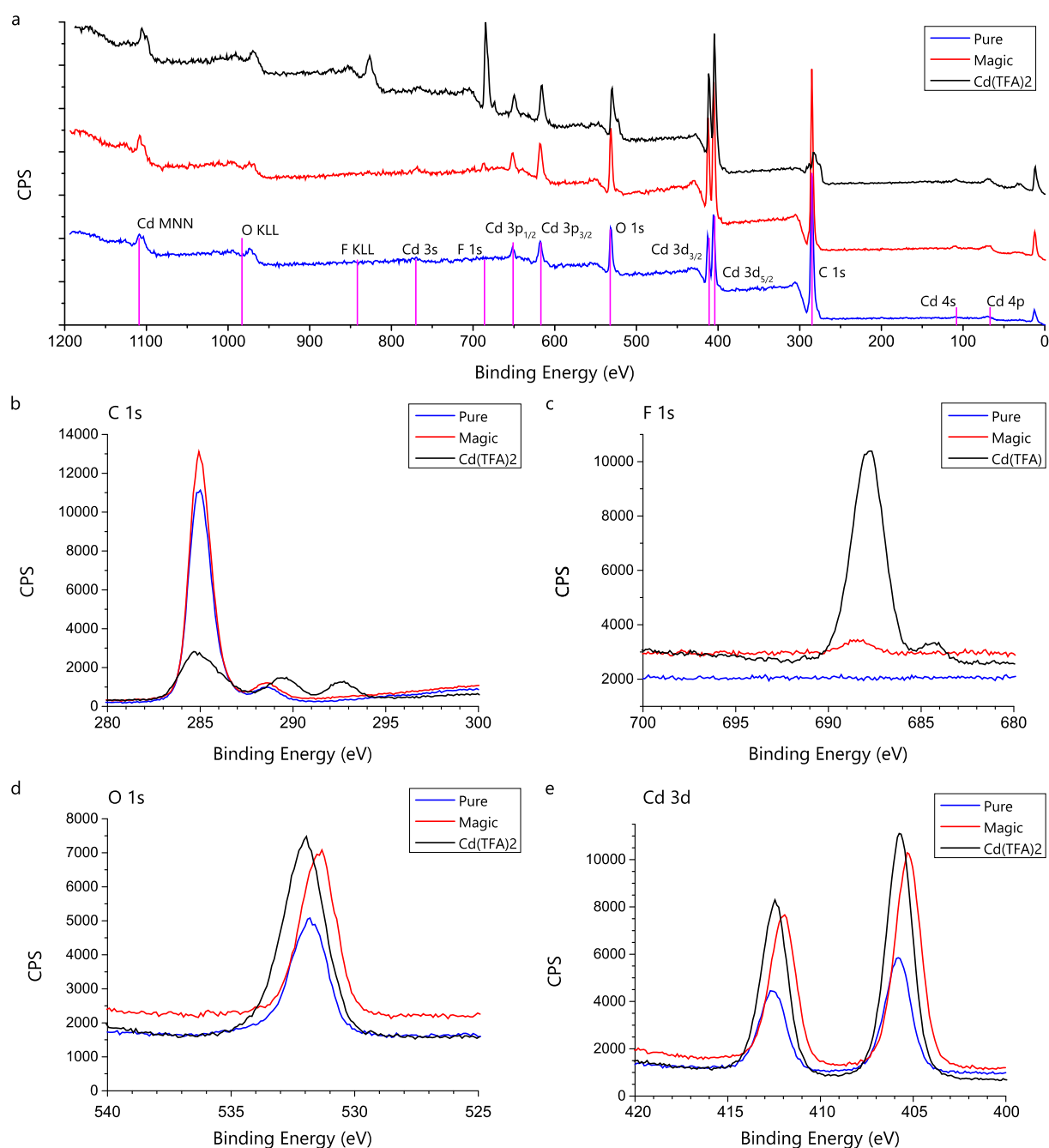
FIGURE 12: **a** survey spectra marking of the element specific signals (magenta) and high resolution spectra of carbon (**b**), fluorine (**c**), oxygen (**d**), cadmium 3d (**e**) for pure, "magic" precursor and Cd(TFA).

For quantification of each element, the high-resolution spectra of the respective areas were recorded. Before analysis, a baseline correction according to Tougaard[34] was performed. Peak fitting using asymmetric Gaussian/Lorentzian curves and integration over the area under each curve was performed (figure 12b-e). In case of the Cd(myristate)$_2$ precursors, carbon is present in the aliphatic and the carboxylate form. For Cd(TFA)$_2$ a typical signal for perfluorinated carbon atoms was found. Three curves

22

are used with fixed distances from the aliphatic peak for carbon. In general, cadmium shows spin coupling of the 3d-Orbital. Thus, the cadmium signal is split into $3d_{3/2}$ and $3d_{5/2}$ and two curves are used to fit the data. For quantification only the integral over the $3d_{5/2}$ signal is used. The spectra are shown in figure 12b to 12e. The atomic percentage of the different species are given in table 1. The stoichiometry was calculated based on this data by dividing the atomic percentage through the amount of cadmium, the value is shown in the lower part of table 1.

TABLE 1: Atomic percentage for cadmium, oxygen, aliphatic carbon, carboxylate carbon, trifluoro carbon, fluorine (upper section) and the stoichiometry calculated over Cd (lower section) of pure and "magic" precursor as for the cadmium trifluoroacetate.

Sample	Cd / at%	O /at%	$C_{aliphatic}$ / at%	$C_{carboxylate}$ / at%	CF_3 / at%	F / at%
"Magic"	5.9	14.4	73.3	5.3	-	1.1
Pure	3.7	12.5	78.1	5.7	-	0.0
$Cd(TFA)_2$	7.5	22.7	26.8	10.6	8.1	22.6
Stoichiometry	Cd	O	$C_{aliphatic}$	$C_{carboxylate}$	CF_3	F
"Magic"	1.00	2.4	12.4	0.9	-	0.2
Pure	1.00	3.4	21.2	1.6	-	0.0
$Cd(TFA)_2$	1.00	3.0	3.6	1.4	1.1	3.0

The "magic" precursor shows a higher cadmium and oxygen content and a lower carbon content compared to the pure cadmium myristate. The presence of fluorine and the different Cd:O:C ratios of the "magic" precursor suggest that the "magic" precursor is contaminated with $Cd(TFA)_2$. A $Cd(TFA)_2$ contamination in $Cd(myristate)_2$ would reduce the relative carbon content and enhance the relative cadmium and oxygen content. Due to the low content of fluorine in the sample, it was not possible to identify perfluorinated carbon atoms. The $Cd(TFA)_2$ control sample shows a rather high concentration of aliphatic carbons, which probably originate from organic contamination from the substrate or from dust in the air.

The value of calculated stoichiometry is low compared to the ideal stoichiometry for all components except for cadmium. This might be due to probe damage by X-ray radiation. But since the damage for all samples should be in the same range, comparisons

between the samples are still valuable. A sum formula can be derived either based on the overall carbon or the overall fluorine count by the stoichiometry of the "magic" precursor assuming that the only feasible fluorine contamination is $Cd(TFA)_2$. Since errors in the carbon signal due to contaminations etc. are likely, the fluorine signals used to derive the formula of the "magic" precursor to $Cd(myr)_{1.93}(TFA)_{0.07}$. Noteworthy, the XPS data does not allow to assess whether TFA is present in the form of $Cd(TFA)_2$ impurity that is mixed with $Cd(myristate)_2$, or if it is present in the form of mixed coordination polymers in the form of $Cd(myristate)_{2-x}(TFA)_x$.

3.3.1.2 THERMOGRAVIMETRIC ANALYSIS AND DIFFERENTIAL SCANNING CALORIMETRY

With XPS available impurities can be analyzed only under UHV, while volatile substances are absent. In contrast, thermogravimetric analysis (TGA) can detect volatile impurities. Complete decomposition of the organic part of the probe can provide information about the metallic content. Phase transitions and possible reactions can be observed through differential scanning calorimetry (DSC). Thermogravimetric analysis was done under air, to promote complete decomposition of the organic components. For better comparability, the relative mass change is plotted against the temperature (figure 13a).
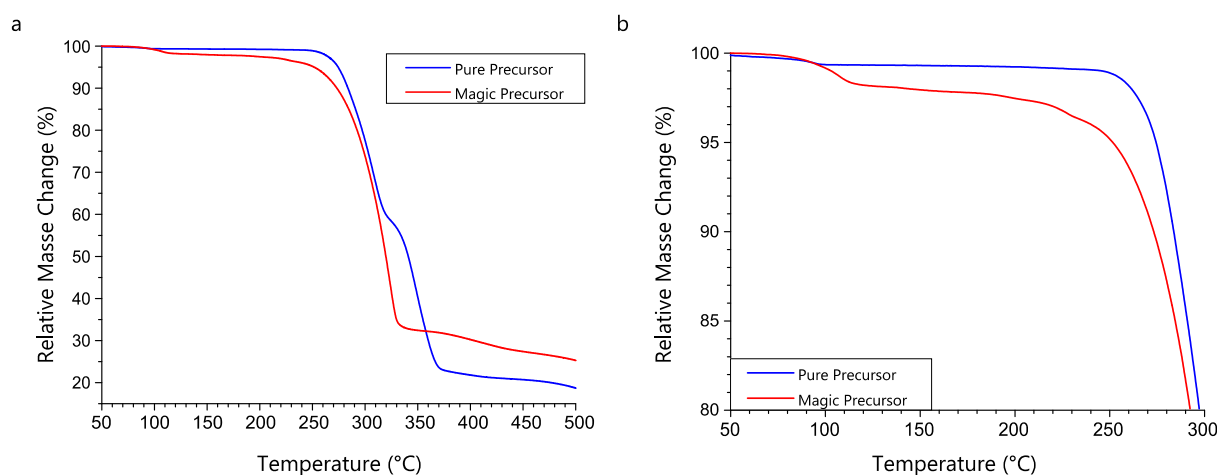
FIGURE 13: Thermogravimetric analyses under air of "magic" (red) and pure precursor (blue). Relative mass change in percentage is plotted against temperature. The full temperature range is given in **a** while **b** shows the range just before decomposition (heating rate at 10 K/min)

Both precursors show a mass loss starting from 100 °C, most likely stemming from the evaporation of water ($T_{b,H_2O} = 100$ °C), triethylamine ($T_{b,TEA} = 89$ °C) or trifluoro acetic acid ($T_{b,TFA} = 72,5$ °C). For pure myristate, this accounts for 0.6 % and for "magic" 1.8 % weight loss at 120 °C. At that point, the "magic" precursor shows steady weight loss

and starts to decompose at lower temperature compared to the pure cadmium myristate (see figure 13b for zoom on the corresponding area). This might be due to the TEA and TFA impurities, which evaporate and even could catalyze the decomposition. The rapid weight loss due to decomposition stops at around 345 °C for the "magic" precursor and for the pure one at 375 °C. At this temperature, all organic molecules should be decomposed to carbon dioxide and water and the cadmium species should have formed non-volatile cadmium oxide. At 400 °C, the relative mass loss for the "magic" precursor is 70 % and for the pure precursor 78 %. With the molar mass of cadmium myristate of 567 g/mol, a relative change of 78 % would yield a molar mass of 125 g/mol. Cadmium oxide has a molar mass of 128 mol/g. Hence, cadmium oxide is the most likely formed compound, assuming some carbon residue and regarding the weight loss in the beginning. In case of the "magic" precursor, the leftover mass is higher, and thus, the cadmium amount should be higher, which supports the assumption that $Cd(TFA)_2$ is present as a major impurity.
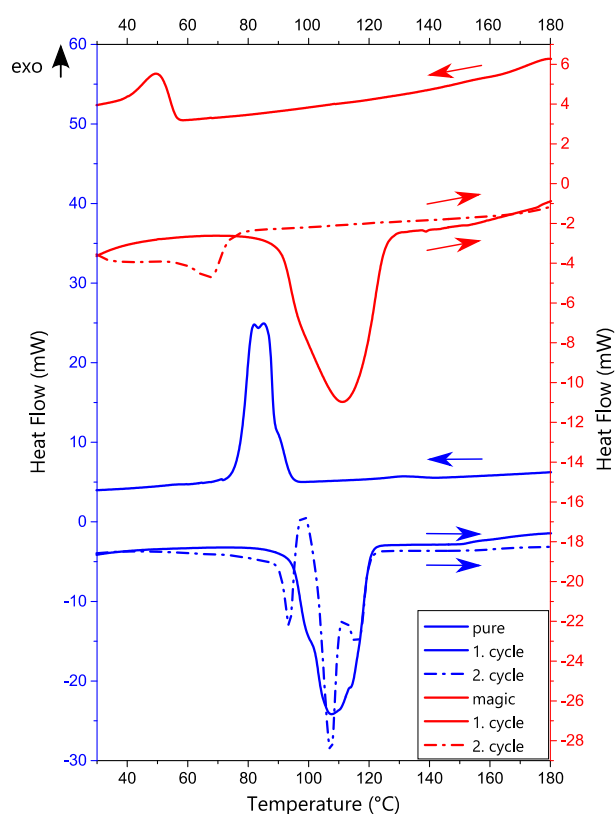
FIGURE 14: Differential scanning calorimetry of "magic" (red) and pure precursor (blue), shown is the power flow from 30 °C to 180 °C (heating rate at 10 K/min)

Using Differential scanning calorimetry, a different behavior for both samples was found, as shown in figure 14. In the first heating cycle, the pure precursor showed a broad endothermic signal from 100 °C to 120 °C. For the "magic" precursor, a similar behavior is observed but starting already at 90 °C and lasting to nearly 130 °C. The endothermic features indicate melting or evaporation in both cases. Additionally, a difference in the cooling curves between both precursors is visible, the pure precursor shows exothermic signals from 90-75 °C, which can be attributed to recrystallization from the melt. The "magic" precursor shows a small exothermic signal around 60 °C. In the second heating step, pure $Cd(myristate)_2$ shows three endothermic peaks indicating a complex melting behavior.[4] In the second heating cycle, the energies for the

"magic" precursor are much lower. DSC measurements suggest that the "magic" precursor does not melt, as the endothermic signal in the first cycle does not reappear, in the second cycle. Thus, it is more likely that a reaction or evaporation during the first cycle took place which changed the samples' properties.

In summary, from thermal analyses a low volatile impurity could be identified in the "magic" precursor, due to the relative mass loss under 100 °C. Additionally, higher residual weight was detected with TGA, which indicates a higher cadmium amount, as already observed by XPS (chapter 3.3.1.1). An endothermic reaction occurred around 110 °C for the "magic" precursor.

3.3.1.3 NUCLEAR MAGNETIC RESONANCE SPECTROSCOPY

Another method to identify potential volatile impurities besides TFA (see chapter 3.3.1.1) is 1H-NMR spectroscopy [1]H-nuclear magnetic resonance spectroscopy (NMR). Afterwards, solid state NMR of different cores [113]Cd, ^{19}F, ^{1}H and [1]H-^{19}F-HOESY (Hetero Nuclear Overhauser Enhancement and Exchange Spectroscopy) is conducted to learn more about their electronic environment. Different or mixed coordination partners for the cadmium should result in different chemical shifts. Additionally, the presence of multiple phases beside the solid cadmium myristate can be identified. The HOESY spectroscopy observes the nuclear Overhauser effect (NOE), that originates from the cross-space dipolar coupling without scalar coupling. Thus, spatially close cores can be identified.
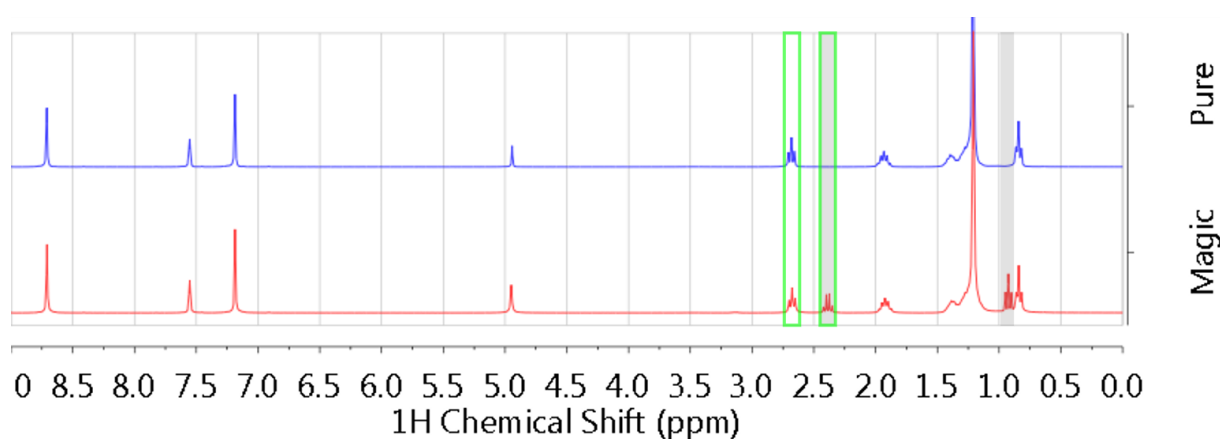
FIGURE 15: ^{1}H-NMR spectra of pure (blue) and "magic" precursor (red), measured at 300 MHz in deuteron pyridine. The areas for triethylamine marked grey.

In the ^{1}H-NMR spectra shown in figure 15, TEA is clearly visible due to the triplet at $\delta = 0.93$ ppm and the quartet at $\delta = 2.39$ ppm (highlighted in grey). From integration

of the signals (green boxes), the molar ratio myristate:TEA can be determined to be 1:0.18. Small amounts of water were also identified by the singlet at 4.94 ppm. The singlet signals at 7.19 ppm, 7.55 ppm and 8.71 ppm originated from pyridine, which was used as solvent. The spectra are scaled to the singlet at 8.71 ppm.
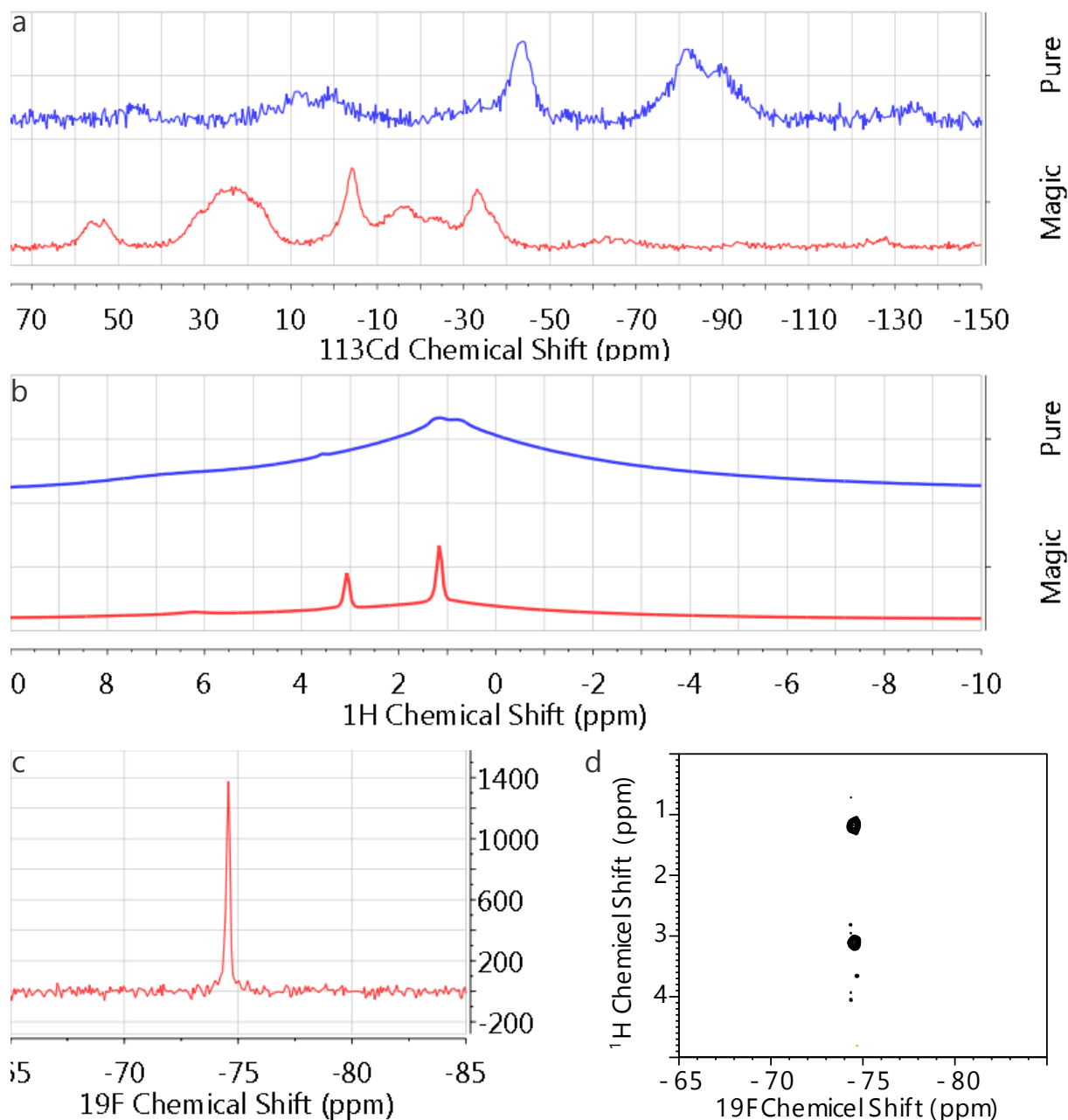
FIGURE 16: ^{113}Cd (MAS at 10 kHz) (**a**) and ^{1}H solid-state NMR spectra (MAS at 25 kHZ) (**b**) of "magic" (red) and pure precursor (blue). ^{19}F solid-state NMR (MAS at 30 kHz) (c) and ^{1}H-^{19}F-HOSEY-NMR (MAS at 30 kHz) (**d**) spectra for "magic" precursor. All spectra measured at 500 MHz.

In solid-state NMR ^{113}Cd, ^{19}F, ^{1}H and ^{1}H-^{19}F-HOESY were measured. ^{113}Cd-NMR spectroscopy indicates a different electronic surrounding for the cadmium in both precursors due to the multiple broad peaks visible in the spectra (figure 16a). Since both spectra show Cd signals of very different chemical shifts it can be concluded that the

binding situation for the pure and the "magic" precursor are different. In ^{1}H-ssNMR spectra (figure 16b), a very broad peak ($\delta = 1$ ppm) is observed for the pure precursor, which arises from the fixed myristate-chains. In the spectra of the "magic" precursors, two sharp singlets ($\delta = 1$ ppm, 3.5 ppm) on top the broad peak are visible and a broad shoulder at $\delta = 6$ ppm. The two sharp singlets correspond to the highly mobile ethyl chains, most likely from the TEA, where the broad shoulder could be due to crystaline water. In ^{19}F-NMR spectra (figure 16c), a sharp singlet at -74 ppm is visible. This indicates a mobile fluorine species, most likely TFA. The ^{1}H-^{19}F-HOSEY NMR spectrum (figure 16d) reveals coupling of the mobile fluorine species and the mobile protons. This indicates a possible spatial close mobile [TEA][TFA] adduct, which might form a second phase.

In summary, from NMR spectroscopy TEA, TFA and their adduct could be identified as impurities. From ^{113}Cd-NMR spectroscopy it could be shown that the cadmium in both samples has a different surrounding. It cannot be differentiated whether these differences came from cadmium trifluoroacetate and myristate or if a mixed cadmium myristate trifluoroacetate salt is present. For differentiation between both types a ^{113}Cd-NMR spectrum of pure cadmium trifluoroacetate is needed.

3.3.1.4 INFRARED-SPECTROSCOPY

Infrared spectroscopy as an ensemble measurement was used to further characterize the binding situation between carbon atoms and their neighbors. It was demonstrated by Mesubi,[35] that information about the binding situation of the carboxylate with the cadmium ion can be obtained from the shifts of the antisymmetric $\nu_a(COO^-)$ and the symmetric stretching mode $\nu_s(COO^-)$ of carboxylates. By carefully analyzing these signals, monodentate and bidentate binding modes can be distinguished. Furthermore, it is possible to distinguish between bridging and chelating binding (scheme 2).

| monodentate structure | chelating bidentate structure | bridging bidentate structure |
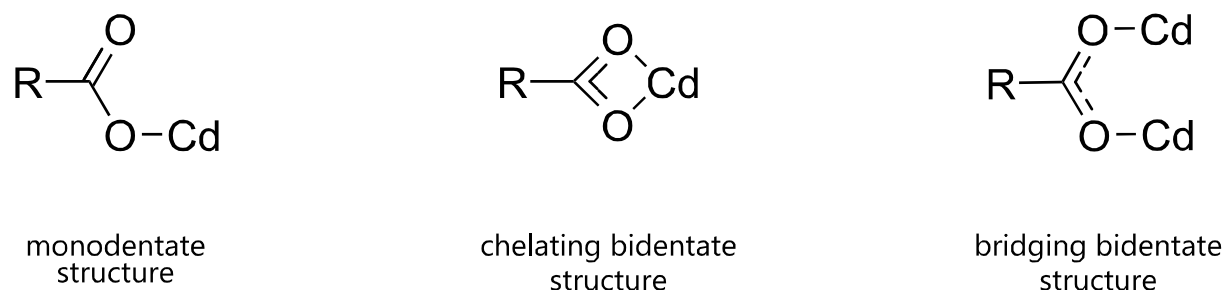
SCHEME 2: Possible biding situation between cadmium and carboxylic groups.[35]

This can be explained by the changes in electron density which depends on the binding situation and the assumption that chemical bonds can be described as a spring in the IR-spectroscopy. Thus, a change in electron density between the atoms results in a change in spring constant between those atoms. In case of monodentate binding, the electron density is spread asymmetrically over the O-C=O for a better charge compensation, where bidentate binding would result in higher symmetry of electron density distribution over the O-C=O. Hence, for bidentate binding a symmetric shift for both vibrational modes in the same direction should be expected, whereas monodentate binding induces an asymmetric shift of both vibrational modes in opposite directions. Shifting of stretching modes are compared to the modes of a "free ion", with sodium myristate as a reference. In case of bidentate binding a further distinction can be made between bridging and chelating, made visible by the difference between $\nu_a(COO^-)$ and $\nu_s(COO^-)$ mode, $\Delta\nu(COO^-)$. In the case of acetates for chelating binding, a difference smaller than 100 cm^{-1} and for bridging binding a difference around 150 cm^{-1} was observed.[36]

The normalized transmission for the pure, the "magic" precursor and Cd(TFA)$_2$ was plotted against the wavenumber in figure 18a. A zoom on the area between 1900 cm^{-1} and 1000 cm^{-1} is shown (figure 18b) for distinguishing between monodentate and bidentate binding to cadmium. The wavenumber of all relevant peaks are given with assignment of the vibrations and $\Delta\nu(COO^-)$ in table 2. Additional literature values for all characteristic vibrations of triethylamine, sodium myristate and trifluoroacetate are given there as well.
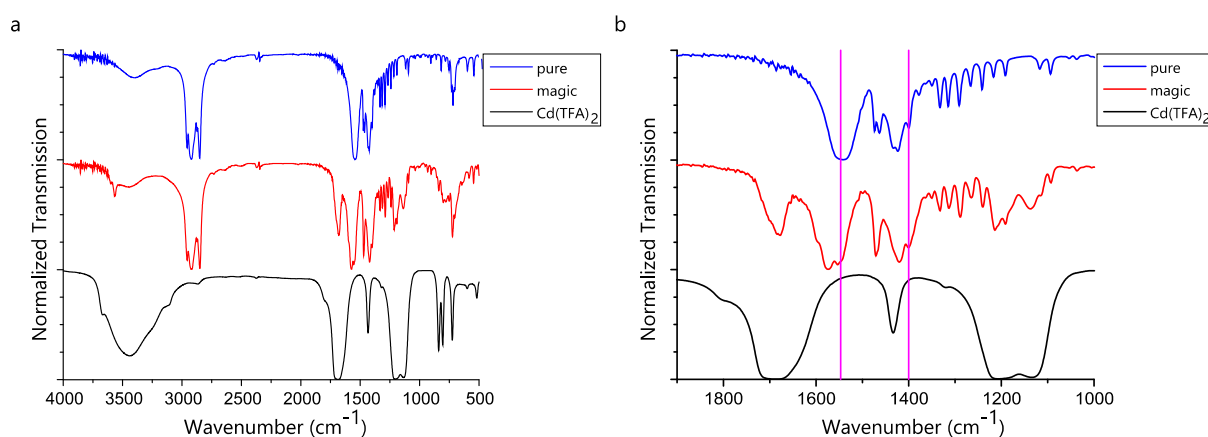
FIGURE 17: Infrared spectra of cadmium trifluoroacetate (black), "magic" (red) and pure precursor (blue) from 4000 cm^{-1} to 500 cm^{-1} (**a**) and form 1900 cm^{-1} to 600 cm^{-1} (**b**). Positions for $\nu_a(COO^-)$ and $\nu_s(COO^-)$ are marked by vertical purple lines.

All spectra show a broad O-H vibration around 3300 cm^{-1}, most likely due to water. The "magic" precursor has an additional sharp band at 3568 cm^{-1}, which indicates a slow or not exchanging COO-H proton. Both precursors show strong bands stemming from stretching of C-H vibrations from the myristate chains from 3000 cm^{-1}. The "magic" precursor shows a peak around 1700 cm^{-1} which is not present in pure cadmium myristate, but present in cadmium trifluoroacetate. For Cd(TFA)$_2$, this peak around 1700 cm^{-1} is the antisymmetric stretching mode of COO$^-$ (v_a), were the symmetric stretching mode of COO$^-$ (v_s) is at 1434 cm^{-1}. The "magic" and pure precursor show the symmetric stretching mode v_s(COO$^-$) at 1400 cm^{-1}. Multiple sharp small bands appear between 1350 cm^{-1} and 1190 cm^{-1} and are associated with wagging or twisting of the CH$_2$ groups. The rocking mode of CH$_2$ is expressed by a band at 720 cm^{-1} and the wagging or twisting features of the CH$_2$ groups show the crystallinity of the hydrocarbon chains like reported for several cadmium fatty acids.[35] The "magic" precursor and the Cd(TFA)$_2$ show an additional band compared to the pure precursor at 1200 cm^{-1} and 1140 cm^{-1}. In this area C-C stretching modes can be observed. For the "magic" precursor, these broad signals might originate from TFA or TEA. Both show the same vibrational mode in this area, so it might be scaffold vibration of an ethyl segments.

TABLE 2: Wavenumbers of all relevant peaks are given with assignment of their vibrational type, for pure, "magic" precursor, cadmium myristate[35], cadmium trifluoroacetate, natrium myristate[37] and triethylamine[38]. For the unassigned peaks from ref. 35, the presence of some peaks is confirmed with a +.

	v_a(COO$^-$)	CH$_3$ asymmetric	v_s(COO$^-$)	Δv(COO$^-$)	v_a(C-C)	v_s(C-C)
Pure	-	1542	1424	1400	142	1217 1192	-
"Magic"	1678	1542	1420	1400	154	1214 1191	1137
Cd(myristate)$_2$.[35]	-	1547	+	1424	135	+/+	-
Cd (TFA)$_2$	1687	-	-	1434	253	1207	1135
Na myristate[37]	-	1559	1447	1424	135	-	-
NEt$_3$[38]	-		1468 1460	-	-	1205	1138

From table 1, shifting in the same direction compared to the "free ion" can be observed for both vibrational modes in both precursors. Thus, the binding situation is bidentate. For the Δv(COO$^-$), a value of 142 cm^{-1} for pure and 154 cm^{-1} for "magic" precursor is observed. A clear distinction between chelating and bridging binding is not possible. In literature, similar results are obtained and an asymmetric bidentate binding is proposed, supported by molar mass measurement.[35] From the higher magnitude Δv for

the "magic" precursor it can be concluded that cadmium trifluoroacetate is present as an impurity.

However, it remains unknown if a mixture of Cd(myristate)$_2$ and Cd(TFA)$_2$ is present, or if the "magic" precursor is a mixed coordination polymer of the type Cd(myristate)$_{2-x}$(TFA)$_x$.

3.3.1.5 Discussion of the Precursor Characterization

The characterization of the "magic" precursor showed different impurities carried over from the precursor synthesis. From XPS, the presence and quantity of fluorine could be determined as Cd(myristate)$_{1.93}$(TFA)$_{0.07}$. Thermal analysis revealed a volatile impurity and a larger residue, ergo a higher relatively cadmium content, as observed in XPS. Instead of melting an endothermic chemical reaction was identified. Liquid NMR confirmed TEA and water as volatile impurities. Solid state NMR identified a second highly mobile phase in the "magic" precursor, which is most likely an adduct of [TEA][TFA]. Different coordination spheres for the cadmium atoms could be confirmed by ^{113}Cd-NMR. Infrared spectroscopy confirmed an asymmetric binding situation for the carboxylic group. Furthermore, cadmium trifluoroacetate could be identified.

TFA is confirmed as an impurity through all applied methods, most likely in a form of cadmium trifluoroacetate. TEA is the second most probable impurity, majorly identified through NMR. Hence, in the next step of the project the influence of the identified impurities in the synthesis of CdSe NPLs was tested by intentionally adding them to the reaction.

3.3.2 Synthetic Results With Addition of Different Impurities

In this chapter the impurities identified in previous chapter 3.3.1 were added during the synthesis of NPL on purpose to study how they affect the formation of NPLs. The influence of impurities on the CdSe NPL reaction was assessed by absorption and photoluminescence spectroscopy of the crude reaction solutions. The addition temperature was changed in following chapter to 200 °C to favor the formation of thicker NPL fractions

3.3.2.1 Triethylamine

Precursors with different TEA content were prepared through reduced washing of the final product as described in chapter 5.3.2. The TEA content was determined by NMR spectroscopy. A precursor with a molar ratio of myristate:TEA of 1:0.23, which is slightly higher than found in the "magic" precursor with 1:0.18, was tested in the standard synthesis (as described in chapter 5.3.3) and yields mainly QDs with small fractions of 3 ML and 4 ML NPLs (figure 18a). This precursor was mixed with pure cadmium myristate to achieve a ratio of 1:0.185, which nearly matches the myristate:TEA ratio for the "magic" precursor (as observed in the NMR experiments, see chapter 3.3.1.3) and was used in synthesis. In the crude spectra, no significant changes to a synthesis with pure myristate (chapeter 3.1, figure 6) were observed (figure 18b).
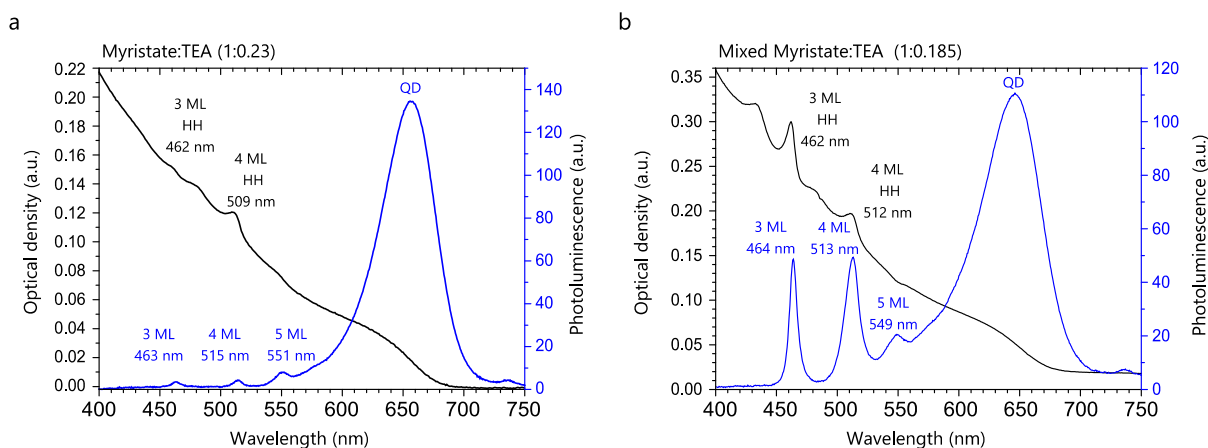
FIGURE 18: Absorption and photoluminescence spectra and the different fraction marked for a precursor with a myristate:triethylamine ratio of 1:0.23 (**a**) and 1:0.185 (**b**).

The reduced NPL formation for the precursor with a ratio of 1:0.23 could be explained by the L-type character of the amine as a ligand,[39] in which only one electron is donated for the coordinative binding. Thereby, TEA weakens the coordination of the carboxylic groups and enhances displacement of cadmium atom on the surface. The displacement in turn raises the surface energy and promotes QD formation. Additionally,

by coordinating to cadmium, TEA also can break the coordination polymer by opening the bridging carboxylate binding modes. This leads to a more diffusion limited growth, hence favoring the QD formation (chapter 2.2).

3.3.2.2 TRIFLUOROACETIC ACID

TFA was added after the degassing of the reaction solution at 110 °C. Volumes of 5 μL and 10 μL were tested (for determination of TFA by XPS compare chapter 3.3.1.1, ssNMR, chapter 3.3.1.3, and IR, chapter 3.3.1.4). For 5 μL, no change in the crude spectra (figure 19a) could be observed besides a relatively broad emission peak of the QD fraction. This signal broadening could be due to overlay of the signal from growing of a 5 ML and 6 ML fraction, which is indicated by the steps, with the QD signal. Using the double amount of TFA yields, only 4 ML NPLs and QDs according to the absorption and photoluminescence spectra (figure 19b).
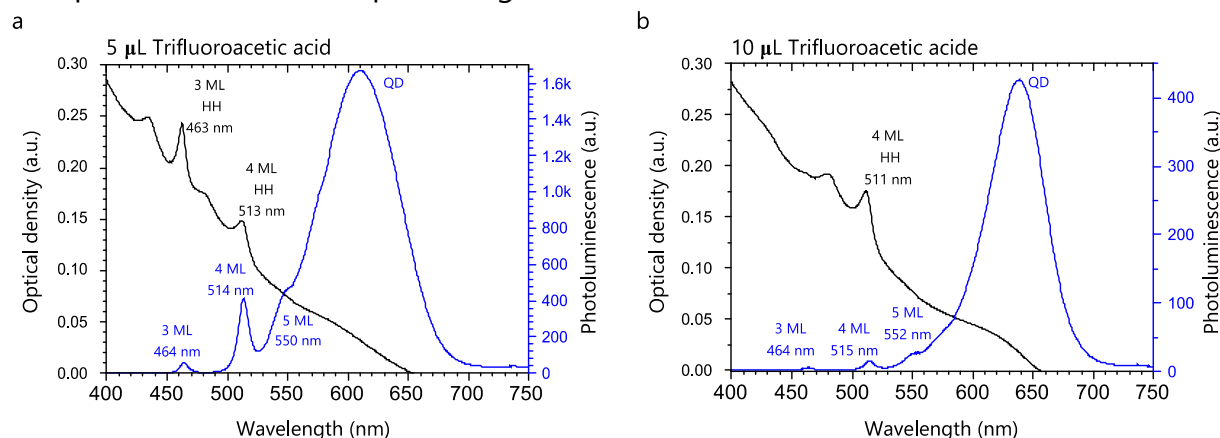
FIGURE 19: Absorption and photoluminescence spectra and the different fraction marked for the addition of trifluoroacetic acid 5 μL (**a**) and 10 μL (**b**).

In both syntheses, a strong steam or smoke evolution over the reaction medium was observable when opening the reaction flask for the addition of cadmium acetate. This might be the boil-off of TFA (boiling point = 72.4 °C), which would lead to uncontrolled reaction. For gaining better control over the actual TFA amount in the synthesis, in the following pure $Cd(TFA)_2$ was added instead of TFA. The use of this compound should be closer to the actual situation in the "magic precursor" as $Cd(TFA)_2$ or mixed $Cd(myristate)_{2-x}(TFA)_x$ was detected in the XPS, ss-NMR and IR experiments.

3.3.2.3 CADMIUM TRIFLUOROACETATE

$Cd(TFA)_2$ could be added to the reaction mixture either in the beginning of the synthesis (together with $Cd(myristate)_2$ and Se), or added together with $Cd(OAc)_2$ at elevated temperatures. In a first series of experiments, $Cd(myristate)_2$ was partially replaced

with 5 mol% and 10 mol% Cd(TFA)$_2$. The absorption and photoluminescence spectra of the final, crude reaction products are shown in figure 20. For 5 mol% (figure 20a) and 10 mol% (figure 20b) of Cd(TFA)$_2$, only small differences compared to the pure cadmium myristate precursor were observed. A close comparison reveals a lower count of all NPL fractions when 10 mol% instead of 5 mol% Cd(TFA)$_2$ were present from the start of the reaction.
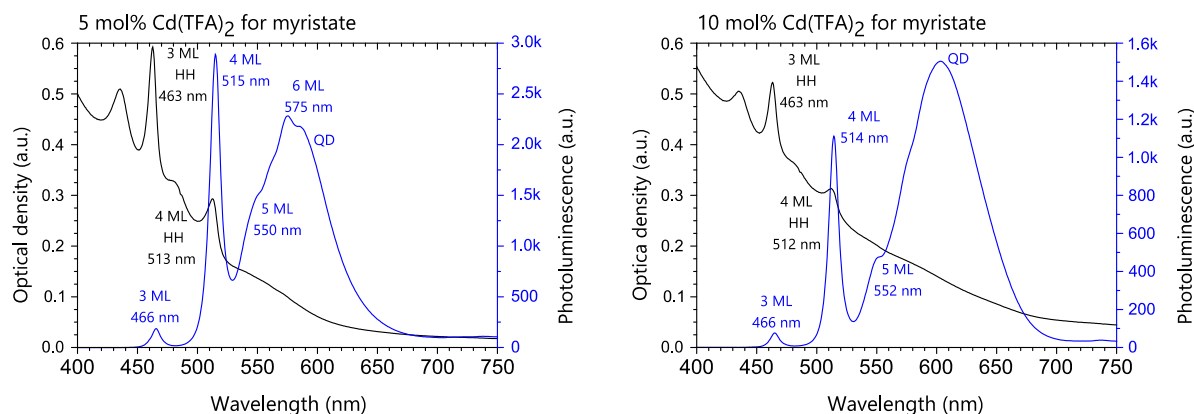
FIGURE 20: Absorption and photoluminescence spectra (with the different fraction marked) for the addition of trifluoroacetate (Cd(TFA)$_2$) with 5 mol% (**a**) and 10 mol% (**b**) as a replacement of cadmium myristate.

Even though in these two experiments the used amounts of Cd(TFA)$_2$ were above the concentration calculation based on the XP-spectroscopy (3 mol%), the influence of Cd(TFA)$_2$ when added at the beginning of the synthesis was limited.

Hence, in the following, Cd(OAc)$_2$ was partially substituted with Cd(TFA)$_2$ and the mixture was added at elevated temperatures to trigger the NPL formation. For this, 25 mol%, 40 mol%, 50 mol%, 75 mol% and 100 mol% of the Cd(OAc)$_2$ were replaced with Cd(TFA)$_2$. The absorption (figure 21a) and normalized photoluminescence spectra (figure 21b) of the final, crude reaction products are shown below.
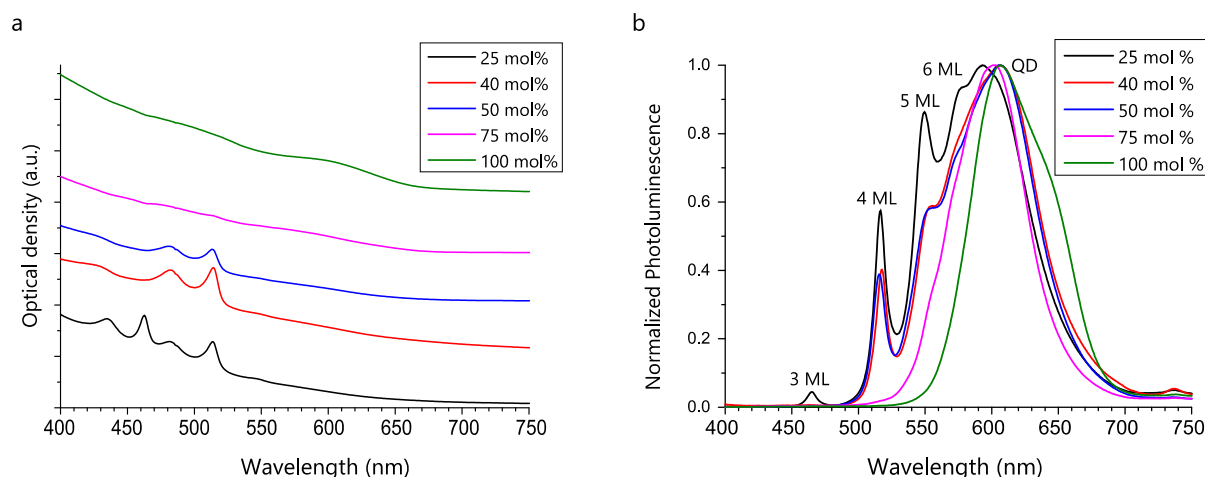
FIGURE 21: Absorption (**a**) and photoluminescence spectra (**b**)with the different fraction marked for the addition of trifluoroacetate (Cd(TFA)$_2$) with 25 mol%, 40 mol%, 50 mol%, 75 mol% and 100 mol% as a replacement of cadmium acetate.

From the spectra of the crude reaction mixtures, significant differences are visible. A replacement with 25 mol% Cd(TFA)$_2$ results in similar 3 ML, 4 ML NPLs, and QD mixtures as the pure precursor. A further increase of the Cd(TFA)$_2$ fraction to 40 mol% and 50 mol% yields only 4 ML thick NPLS, and 3 ML NPLs are absent. In photoluminescence, a 5 ML thick fraction can be observed by the shoulder around 550 nm, but no 3 ML thick NPLs are found. Increasing Cd(TFA)$_2$ to 75 mol% or 100 mol% yields almost exclusively QDs, wherein in the photoluminescence spectra for the 75 mol% sample a very weak shoulder around 550 nm is visible, indicating that extremely small amounts 5 ML thick NPLs might be present.

3.3.2.3.1 Replacement of Cadmium Acetate With 25 mol% Cadmium Trifluoroacetate

For a deeper understanding of the differences in growth dynamics, aliquots of all syntheses were analyzed spectroscopically. The absorption (figure 22a) and normalized photoluminescence spectra (figure 22b) are shown below. Additionally, the wavelength of the absorption peak for NPLs of 3 and 4 MLs versus time is shown in figure 22c.
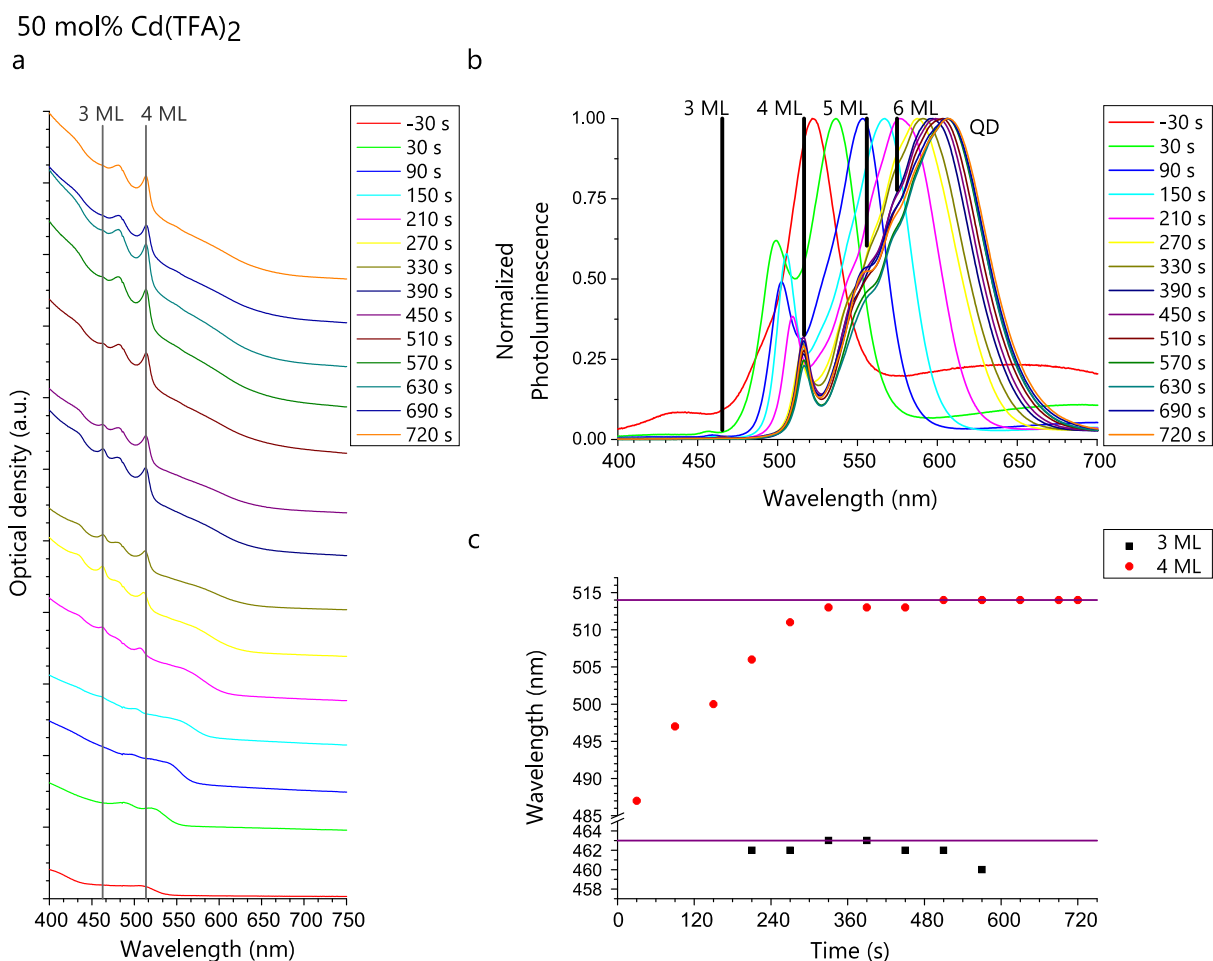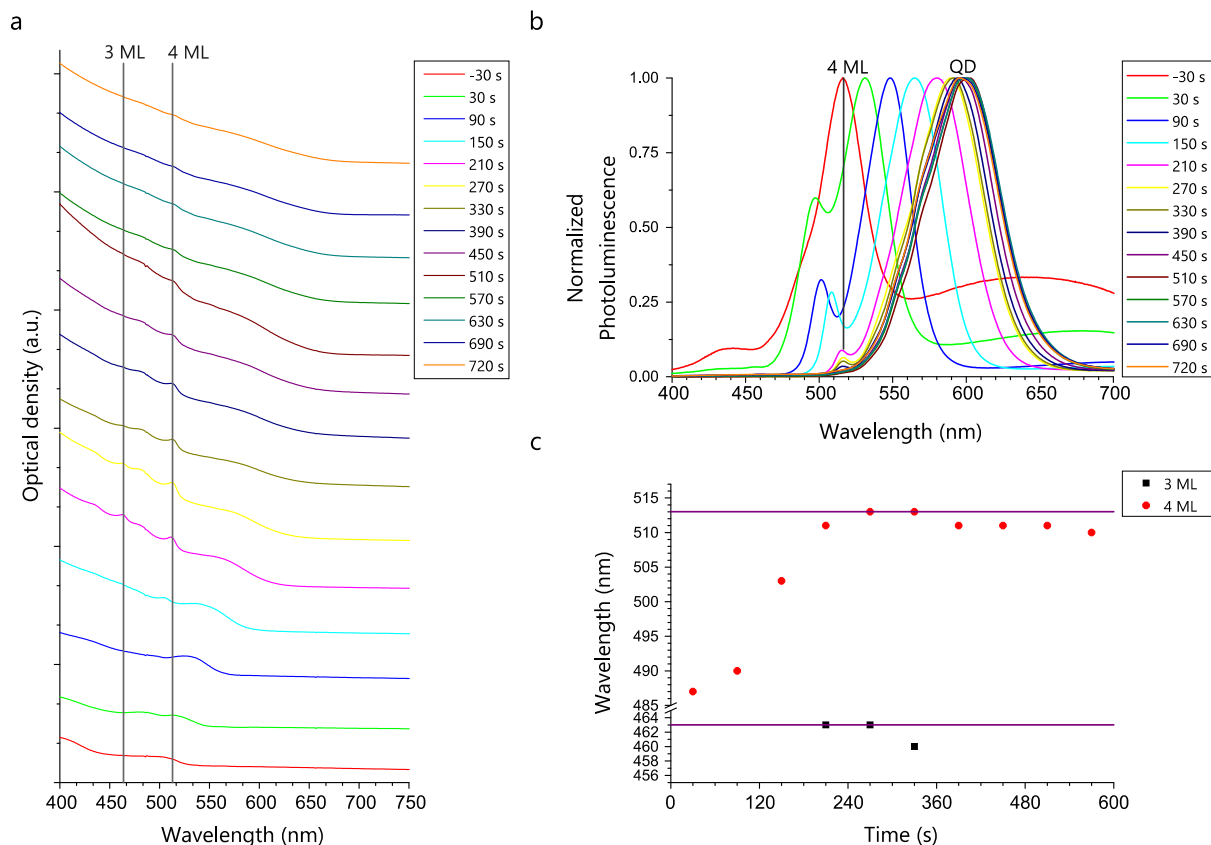
35
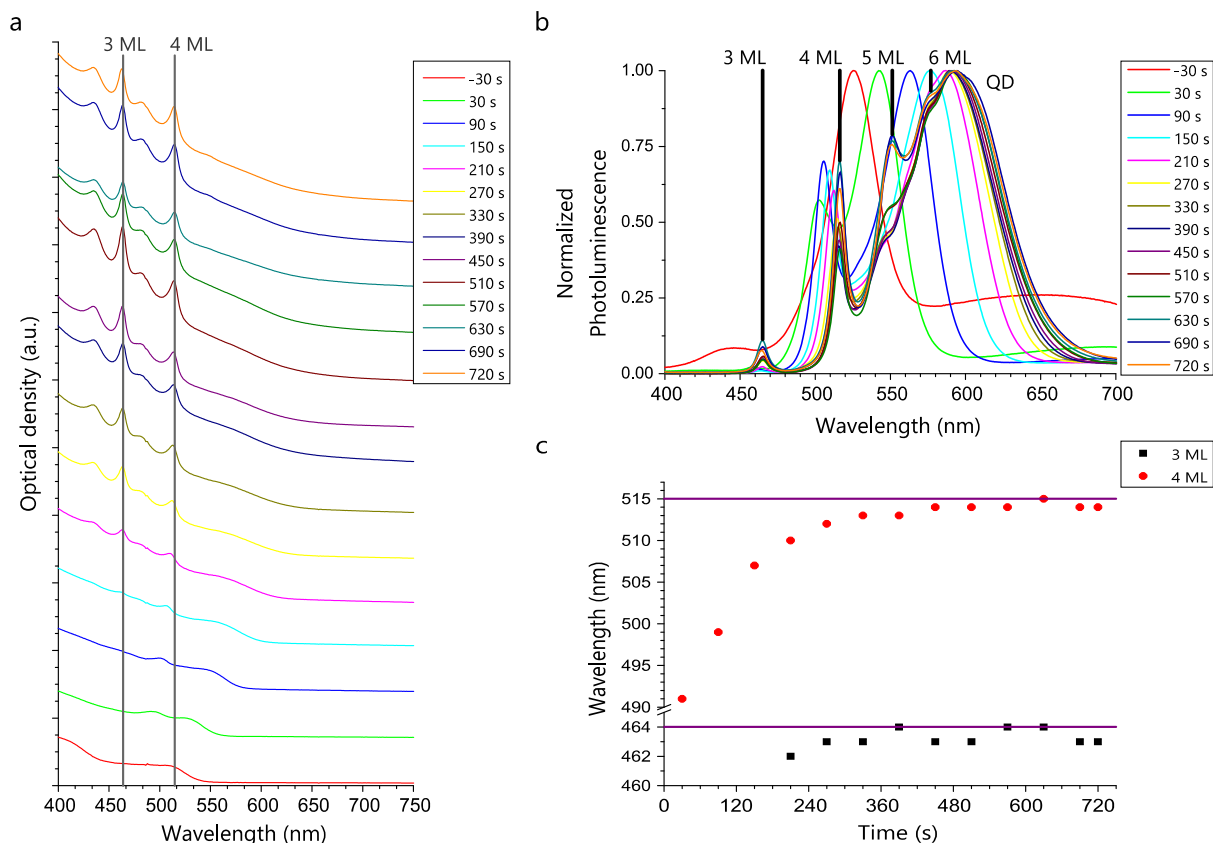
25 mol% Cd(TFA)$_2$

FIGURE 22: **a** Temporal evolution of absorption spectra for the synthesis with 25 mol% Cd(TFA)$_2$. The vertical grey lines indicate 3 ML and 4 ML absorption maxima. **b** Temporal evolution of photoluminescence spectra. The black lines indicate the luminescence maxima for QDs, and 3, 4, 5, and 6 ML nanoplatelet fractions. **c** Temporal evolution of observed absorption maxima for 3 ML and 4 ML thick nanoplatelets over the course of time. The horizontal purple lines indicate the maximum wavelength for NPLs larger than the Bohr radius of the respective fraction.

For the evolution of the absorption and photoluminescence spectra, no difference compared to a normal synthesis can be observed (figure 10, chapter 3.2.3.1). In figure 23c, the growth of the 3 and 4 ML NPLs can be followed over time. First, laterally small 4 ML NPLs with a blue-shifted heavy-hole absorption maximum around 490 nm form shortly after addition of the Cd(OAc)$_2$/Cd(TFA)$_2$ mixture at elevated temperatures. With progressing time this maximum shift to 514 nm (the maximum red-shift observed for 4 ML NPLs with lateral sizes larger than the Bohr radius). For the 3 ML fraction, clear shifting of the absorption peak maxima cannot be observed.

Replacing 40 mol% and 50 mol% of Cd(OAc)$_2$ with Cd(TFA)$_2$ resulted in a 4 ML NPLs and QDs only. Hence, 3 ML NPLs were either, never formed in the synthesis or disappeared over the course of the reaction. For a deeper insight, the absorption and photoluminescence spectra for the aliquots taken during the reaction were recorded as shown below.
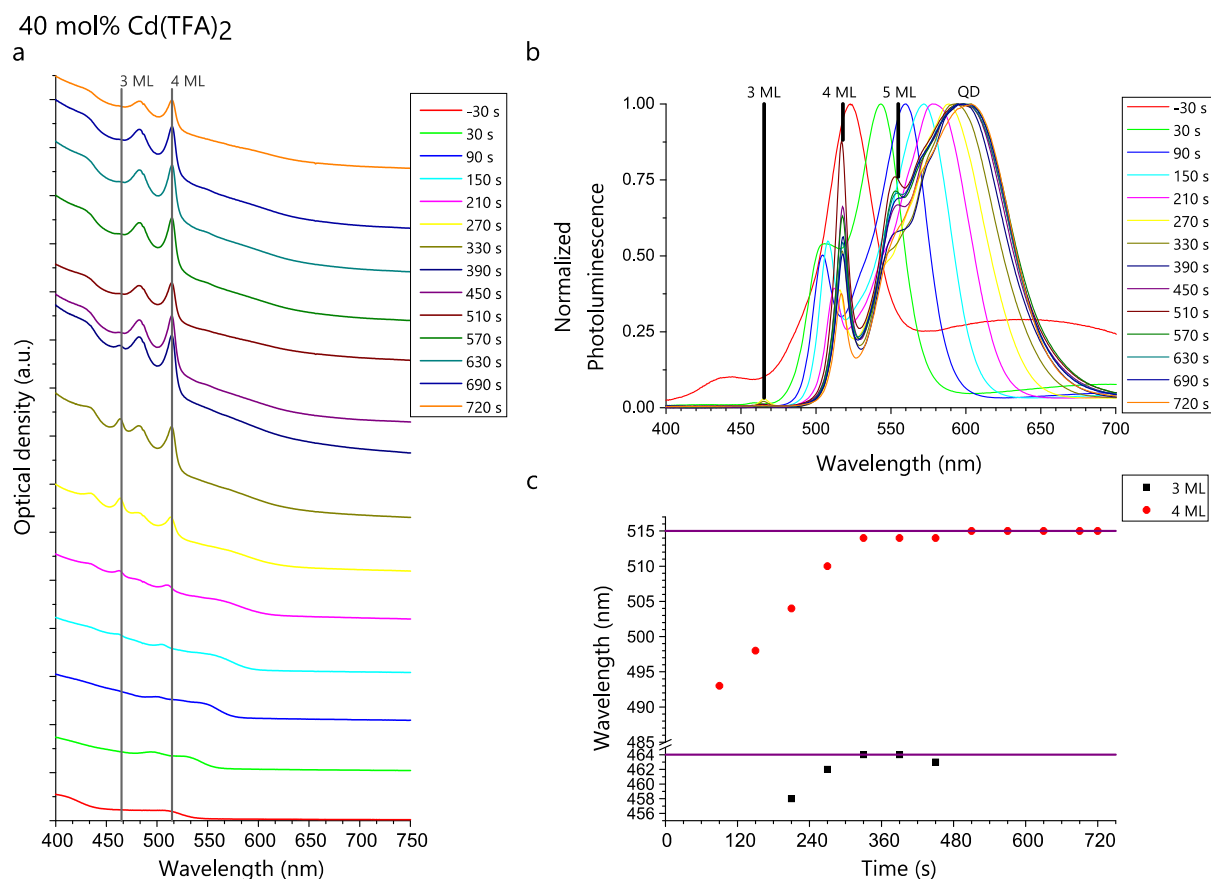
FIGURE 23: **a** Temporal evolution of absorption spectra for the synthesis with 40 mol% Cd(TFA)$_2$. The vertical grey lines indicate 3 ML and 4 ML absorption maxima. **b** Temporal evolution of photoluminescence spectra. The black lines indicate the luminescence maxima for QDs, and 3, 4, and 5 ML nanoplatelet fractions. **c** Temporal evolution of observed absorption maxima for 3 ML and 4 ML thick nanoplatelets over the course of time. The horizontal purple lines indicate the maximum wavelength for NPLs larger than the Bohr radius of the respective fraction.

The absorption (figure 23a) and normalized photoluminescence spectra (figure 23b) for the 40% Cd(TFA)$_2$ sample reveal that indeed 3 ML and 4 ML NPLs were initially formed, as shown by peaks at 464 and 515 nm respectivelly. However, over time the 3 ML NPL absorption decreased in intensity and vanished completely approximatelly 500 s after addition of the Cd(OAc)$_2$/Cd(TFA)$_2$ mixture. In the photoluminescence, at later times traces of 5 ML and 6 ML NPLs can be observed. Following the heavy hole transition peak shifts for the 3 ML and 4 ML fractions over time (figure 23c) first blue

shifted features of 4 ML than of 3 ML NPLs appear. The 3 ML NPL fraction shows initially a peak position, centered around 460 nm at 150 s, which first shifts to 463 nm corresponding to 3 ML NPLs with lateral dimensions larger than the Bohr radius. Over the further course of the synthesis, this peak starts to blue-shift until the peak vanishes. Noteworthy, the blueshift of the 3 ML fraction occurred in response to the 4 ML fraction reaching 514 nm (4 ML NPLs with lateral dimensions larger than the Bohr radius). This behavior – dissolution of the thinner NPLs with simultaneous growth of the thicker NPLs and QDs – is a clear indicator for Ostwald-type ripening.[31]

3.3.2.3.3 REPLACEMENT OF CADMIUM ACETATE WITH 50 MOL% CADMIUM TRIFLUOROACETATE

For synthesis with 50 mol% $Cd(TFA)_2$ a similar behavior was observed. In the evolution of absorption (figure 24a) and normalized photoluminescence spectra (figure 24b) only minor differences to the synthesis described before with 40 mol% $Cd(TFA)_2$ could be detected. The direct comparison of the photoluminescence spectra reveal that the dissolution of the 3 ML NPL fraction appears to be slightly faster. Following, the heavy hole transition peak shifts for the 3 ML and 4 ML fractions over time (figure 24c) showing again the growth of the 4 ML thick NPL fraction from around 490 nm to 514 nm, with simultaneous blue-shifting of the 3 ML thick fraction before complete disappearance.

50 mol% Cd(TFA)$_2$

FIGURE 24: **a** Temporal evolution of absorption spectra for the synthesis with 50 mol% Cd(TFA)$_2$. The vertical grey lines indicate 3 ML and 4 ML absorption maxima. **b** Temporal evolution of photoluminescence spectra. The black lines indicate the luminescence maxima for QDs, and 3, 4, 5, and 6 ML nanoplatelet fractions. **c** Temporal evolution of observed absorption maxima for 3 ML and 4 ML thick nanoplatelets over the course of time. The horizontal purple lines indicate the maximum wavelength for NPLs larger than the Bohr radius of the respective fraction.

These experiments thus clearly indicate that a certain concentration of Cd(TFA)$_2$ (or TFA) helped to generate a final product containing only one NPLs thickness fraction by promoting ripening of the thinner NPL fractions.

3.3.2.3.4 REPLACEMENT OF CADMIUM ACETATE WITH 75 MOL% CADMIUM TRIFLUOROACETATE

A further increase in the Cd(TFA)$_2$ amount resulted in almost complete suppression of NPL formation. While at the final stage of the syntheses for both the 75 mol% and the 100 mol% Cd(TFA)$_2$ sample no NPLs were visible in the absorption and photoluminescence spectra, at intermediate times during the synthesis, traces of 3 and 4 ML NPLs were visible (figure 25a and b).

75 mol% Cd(TFA)$_2$

FIGURE 25: **a** Temporal evolution of absorption spectra for the synthesis with 75 mol% Cd(TFA)$_2$. The vertical grey lines indicate 3 ML and 4 ML absorption maxima. **b** Temporal evolution of photoluminescence spectra. The black lines indicate the luminescence maxima for QDs and 4ML nanoplatelet fraction. **c** Temporal evolution of observed absorption maxima for 3 ML and 4 ML thick nanoplatelets over the course of time. The horizontal purple lines indicate the maximum wavelength for NPLs larger than the Bohr radius of the respective fraction.

In the evolution of absorption and normalized photoluminescence spectra, the appearance of 4 ML thick NPLs could be confirmed, while 3 ML thick NPLs were only detectable in the absorption spectra. Following the heavy hole transition peak shifts for the 3 ML and 4 ML fractions over time (figure 25c), again the blueshift of the 3 ML thick NPL fraction can be observed. Additionally, a similar behavior is observed for the 4 ML thick fraction at later time points. When the maximum for 4 ML NPLs is reached (514 nm), the peak slowly blue-shift until vanishing completely after reaching 510 nm. The blueshift of the 3 ML fraction starts after the absorption peak of the 4 ML fraction reached 513 nm.

This experiment proves a compelling point: Cd(TFA)$_2$ (or TFA) acts as ripening agent in a concentration-dependent manner. When added in small amounts, mainly the thinner NPLs are affected. They can dissolve and the released CdSe "monomers" can add to

the next thicker fraction of NPLs or to QDs. When larger amounts are added, all NPLs dissolve and the released CdSe material only adds to QDs. This is obvious when Cd(OAc)$_2$ is completely replaced by Cd(TFA)$_2$.

3.3.2.3.5 REPLACEMENT OF CADMIUM ACETATE WITH 100 MOL% CADMIUM TRIFLUOROACETATE

The evolution of absorption and photoluminescence spectra for full replacement is shown in figure 26. The absence of NPL fractions at any stage of the synthesis can be rationalized by the ripening of NPL seeds before they have a chance to develop clearly into NPLs in decent concentrations.
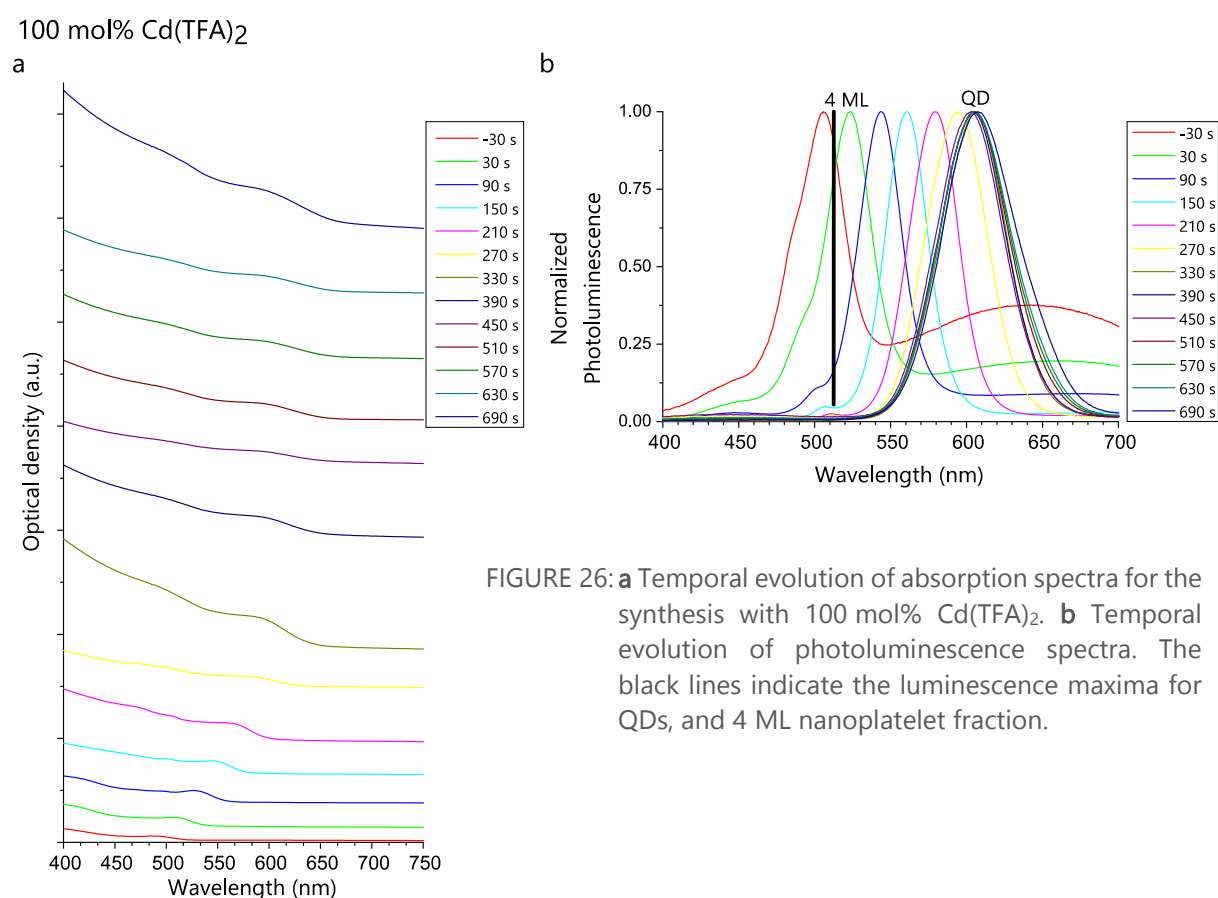
100 mol% Cd(TFA)$_2$

FIGURE 26: **a** Temporal evolution of absorption spectra for the synthesis with 100 mol% Cd(TFA)$_2$. **b** Temporal evolution of photoluminescence spectra. The black lines indicate the luminescence maxima for QDs, and 4 ML nanoplatelet fraction.

In the absorption spectra (figure 26a), only the appearance and shifting of a shoulder can be observed, which is the QD fraction. In the normalized photoluminescence (figure 26b) a minimal amount of 4 ML fraction is indicated by a shoulder around 490 nm. This 4 ML fraction later formed a small peak around 505 nm but vanished completely until the end of the reaction. Overall, too large amounts of Cd(TFA)$_2$ (or TFA) accelerate ripening of NPL nuclei tremendously resulting in formation of only QDs.

3.3.2.4 Discussion of Impurities in Typical Cadmium Selenide Nanoplatelet Syntheses

By testing the identified impurities TEA and TFA/Cd(TFA)$_2$ in typical CdSe NPL syntheses it became clear that TFA/Cd(TFA)$_2$ had the biggest influence for the formation of majorly NPLs. TEA seems to influence the formation of NPLs mainly through dissolution of the cadmium coordination polymers – thus propelling the reaction into the classical diffusion limited regime – leading to increasing amounts of QDs with increasing amounts of TEA, but without significantly changing the typical ratios between different NPL thickness fractions. Instead, the addition of TFA/Cd(TFA)$_2$ to the reaction mixture results in elimination of thinner NPLs at intermediate concentrations and at high concentrations in elimination of all NPLs. The concentration-dependent elimination of thinner NPLs with simultaneous growth of the thicker NPL fractions and QDs can be attributed to Ostwald-like ripening. Here, thermodynamically favored sub-populations, namely thicker NPLs and QDs, grow at the expenses of the thermodynamically less favored subpopulations of thinner NPLs over the course of the synthesis.

These findings are in contrast to recent discoveries for chloride impurities in the synthesis of CdSe NPLs.[23] It was found that chloride attenuates the formation enthalpy of CdSe "monomers" and is not involved with changes to surface energies. Thus, according to the model by Riedinger *et al.*[4], the addition of chloride modifies the volume energy E_V (in other words, the chemical potential) rather than the surface and edge energies E_A and E_L. In contrast, according to my findings described in this work, the addition of TFA/Cd(TFA)$_2$ clearly modifies the ripening behavior. This result proves clearly that these impurities are inducing changes to the surface and edge energies E_A and E_L. These energetic changes modify the distribution of NPL thickness fractions through Ostwald-like ripening processes rather than through changes to the CdSe "monomer" formation enthalpies.

Taken all together, one can conclude that three types of impurities exist that influence the synthesis of CdSe NPLs in different ways. Amines, such as TEA, can break down cadmium coordination polymers and thus drive the reaction towards the classical diffusion limited growth. In such cases, with increasing amine concentrations, increasing amounts of QDs and less amounts of NPLs are formed, while the relative NPL thickness distribution is not altered significantly. Halogenides, introduced in the form of CdCl$_2$ can modify the reaction by altering the formation enthalpy of CdSe "monomers".[23] In such cases the size dependent island nucleation barriers can be modified by changing the chemical potential. Strong carboxylic acids such as TFA, introduced *e.g.* in the form

of Cd(TFA)$_2$, alter the surface and edge energies of the NPLs and thus can promote thickness-selective Ostwald ripening. This finding will later allow for syntheses where at the end only one NPL fraction is present, significantly simplifying consecutive separation protocols (size-selective precipitation).

3.4 Differences "Magic" Precursors to Intentionally Doped Systems

The behavior of the "magic" precursor, the absence of 4 ML thick NPL and 5 ML thick NPL as main fraction, could not be reproduced, but a similar behavior with only a 4 ML thick fraction could be synthesized through doping with TFA/Cd(TFA)$_2$.

The growth of nanoplatelets can be described, in accordance to the kinetic growth instability by Riedinger *et al.*[4] as follows: Normal homogeneous nucleation lead to the formation of spherical QDs. The QD fraction grows over time and with the growth optical features (absorption and photoluminescence peak) redshift. Under the reaction condition with the high cadmium precursor concentration, the overall growth rate is no longer diffusion limited. The QD fraction grows and if QD with a diameter similar to the thickness of a given NPL fraction are available, a rapid lateral growth occurs after stochastic symmetry breaking. Nanoplatelet seeds with rectangular shapes are formed and grow rapidly at the narrow facets.

In the "magic" precursor, the growth of 4 ML thick NPLs is suppressed or just screened, due to a lower island nucleation barrier which favors the next thicker fraction. The occurring 3 ML thick nanoparticles might be explained by a second nucleation event, initialized by the cadmium acetate addition. The occurring ripening is similar to the one observed for magic sized CdSe clusters[32], because the dissolving fraction of 3 ML does not undergo blue shifting of the absorption maximum.

However, in the replication *via* Cd(TFA)$_2$ addition, differences were observed. Firstly, only 4 ML and not 5 ML thick NPLs are formed, second, the needed amount of fluorine impurity is at least ten times higher than the concentration in the "magic" precursor. The observed ripening is Ostwald-like suggested by a blue shift of the dissolving 3 ML fraction, which indicates lateral shrinking of NPLs. This leads to the assumption that a changed surface energy γ, E_A and E_L respectively, is the driving force underneath this observation. For the "magic" precursor, the formation of nearly only a 5 ML thick NPL fraction might be explained due to changes in the monomer formation energy E_V, similar to the observation with chloride impurities, reported and explained by Talapin *et*

al.[23] Further experiments might be conducted to reproduce the influence on the formation energy, this might be realized with mixed cadmium myristate trifluoroacetate coordination polymers.

4 CONCLUSION

The aim of this work was to probe the influence of impurities on the growth of CdSe NPLs. First attempts of *in situ* absorption and photoluminescence spectroscopy *via* dip probes were not successful, mainly due to technical issues (gas bubbles), extensive thermal peak broadening, and thermal photoluminescence quenching. However, by employing *ex situ* spectroscopy of aliquots collected during the growth, the influence of impurities could be assessed reliably. By employing a series of suitable analytical methods, I could identify common impurities found in $Cd(myristate)_2$ precursors. These were identified to be TEA and $TFA/Cd(TFA)_2$. By intentionally adding these impurities to the CdSe NPL synthesis, I could show that both types of impurities influence the growth of CdSe NPLs, but *via* different pathways. TEA can break down the cadmium coordination polymers and drive the reaction towards the diffusion limited growth, resulting the enhanced formation of QDs at the expense of NPLs. In contrast, $TFA/Cd(TFA)_2$ apparently modifies the surface and edge energies of NPLs in the system and acts in concentration-dependent manner as Ostwald-ripening agent.[31] I demonstrated that with this impurity it is possible to obtain only one thickness fraction of NPLs (here shown for 4 ML NPLs) at the end of the synthesis. This findings are beneficial for CdSe NPL synthesis, as the cumbersome separation of NPLs with different thicknesses by size-selective precipitation can be avoided. Additionally, these findings add new knowledge to the overall understanding of CdSe NPL growth.

Even though the careful analysis of the "magic" precursor – a batch of $Cd(mysistate)_2$ that behaved notably differently from all other $Cd(myristate)_2$ batches – revealed the TEA and $TFA/Cd(TFA)_2$ impurities, the intentional addition of these impurities to the CdSe NPL synthesis did not yield exactly the same results as the "magic" precursor. This implies that in the "magic" precursor $Cd(TFA)_2$ is not simply blended with $Cd(myristate)_2$. Most likely TFA is present in a form of mixed coordination polymers of the type $Cd(myristate)_{2-x}(TFA)_x$. Thus, future experiments should take these findings into account and aim for the targeted synthesis of $Cd(myristate)_{2-x}(TFA)_x$ compounds with various TFA contents.

The presence of mixed coordination polymers could be addressed by comparison of additional ^{1113}Cd-ssNMR measurements of $Cd(TFA)_2$, $Cd(myristate)_2$ and the "magic" precursor. Further, the influence of differently substituted carboxylates on the formation energy could be tested. Due to easy tailoring of the binding strength of carboxylate group to the cadmium *via* variation of the substituents at the carboxylate, (*e.g.*

mono-, dichloroacetic acid or cyanoacetic acid) should be feasible. The already established system could be tested with different reactions parameters, like a change temperature program or addition temperature, to focus the growth of other NPL thickness fractions.

5   METHODS

5.1   Chemicals

Cadmium oxide (≥99.99 %, Sigma Aldrich), Cadmium nitrate tetrahydrate(98 %, Aldrich), Myristic acid (≥98 %, Sigma-Aldrich) and Oleic acid (90 %, Sigma Aldrich) were purchased from Sigma-Aldrich. Cadmium acetate dihydrate (98 %, Acros) and 1-Ocatadecene (90 %, Acros) were purchased from Acros Organics. Selen powder (99.999 %, Alfa Aesar) and Trifluoroacetic anhydride (99+ %, Alfa Aeasar) were purchased from Alfa Aesar. Hexane (≥95 %, Fluka), Isopropanol (≥99.5 %, Fluka) and Triethylamine (99.5 %, Fluka) were purchased by Fluka Research Chemicals. Acetonitrile (99.9 %, Fisher) was purchased by Fisher scientific. Methanol (HPLC grade, VWR) was purchased by VWR chemicals. Sodium Myristate (>98.0 %, TCI) was purchased from Tokyo Chemical Industry. Trifluoroacetic acid (99 %, Merck) was purchased from Merck KGaA. All chemicals were used as purchased.

5.2   CHARACTERIZATION

5.2.1   ABSORPTION AND PHOTOLUMINESCENCE SPECTROSCOPY

For optical spectroscopy, NPL dispersions were transferred to a quartz glass cuvette (10mm). Photoluminescence spectra were recorded using a Prizmatix Silver high power LED (emission peak 369 nm) for excitation. For Absorption spectroscopy an AvaLight-DH-S-BAL light source was used. Avantes SensLine AvaSpec-HSC1024x58TEC-EVO (HSC04000-9.55, Slit-25-RS, OSK-305) was used for data collection.

5.2.2   ABSORPTION AND PHOTOLUMINESCENCE SPECTROSCOPY - *IN SITU*

For *in situ* photoluminescence spectroscopy, a modified Hellma-Analytics Espada Sonde 661-7199-UVS-1.8m-46 as dip probe, a Prizmatix Silver high power LED (emission peak 369 nm) for excitation and Avantes SensLine AvaSpec-HSC1024x58TEC-EVO (HSC04000-9.55, Slit-25-RS, OSK-305) for data collection were used. For *in situ* absorption spectroscopy Ocean Optics TI300-UV-VIS as dip probe, Avantes SensLine AvaSpec-HSC1024x58TEC-EVO (HSC04000-9.55, Slit-25-RS, OSK-305) for data collection and a Prizmatix ultra high power with light LED (UHP-M-DualLED, UV emission peak 405 nm) was used as a light source.

5.2.3   X-RAY PHOTON SPECTROSCOPY (XPS)

X-ray photon spectroscopy was conducted with a Kratos AXIS Ultra DLD with a pump time of 5.5-6 To reduce possible changes in sample composition, first high-resolution

measurement on the area for the O 1s and C 1s spectral regions was performed, followed by F 1s, Cd 3p, Cd 3d spectra and a survey spectrum. For qualitative and quantitative analyses, the CasaXPS V2.3.19 software with the integrated databases were used.

5.2.4 DIFFERENTIAL SCANNING CALORIMETRY (DSC)/ THERMOGRAVIMETRIC ANALYSIS (TGA)

Differential scanning calorimetry and thermogravimetric analysis were conducted on 10 mg samples in a 40 μL alumina crucibles. DSC was performed under N_2-atmosphere on a DSC 823 by METTLER-TOLEDO. TGA was performed under air with a TGA/DSC 3+ by METTLER-TOLEDO.

5.2.5 NUCLEAR MAGNETIC RESONANCE SPECTROSCOPY (NMR)

Liquid NMR measurements were performed in deuterated pyridine in a Bruker 300 MHz spectrometer. For solid-state NMR measurements, a Bruker 500 MHz spectrometer was used, where for cadmium spectra a rotor with a frequency of 10 Hz was used. All analyses were done with Mnova V12.0 from Mestrelab Research S.L..

5.2.6 IR-SPECTROSCOPY

For infrared spectroscopy, 4 mg of a cadmium precursor and 200 mg potassium bromide were mortared. 150 mg of this mixture was pressed to tablets with 125 bar pressure for 7 min. Spectra were recorded form 4000 cm^{-1} to 400 cm^{-1} with a Perkin Elmer FT-IR System Spectrum BX.

5.3 SYNTHETIC METHODS

5.3.1 SYNTHESIS OF CADMIUM MYRISTATE – FROM CADMIUM NITRATE

Cadmium myristate was synthesized starting from cadmium nitrate tetrahydrate according to a modified procedure described by Yang *et al.*[40]. In a 300 mL Erlenmayer flask, cadmium nitrate tetrahydrate (7.8 mmol; 2.46 g) was dissolved in methanol (80 ml). In a 1 L beaker, sodium myristate (24.3 mmol; 6.2 g) was dissolved in 600 mL methanol. The cadmium nitrate solution was added through a dropping funnel into the sodium myristate solution while stirring over a period of 30 min. After stirring for additional 60 min, the colorless precipitate was filtered and was washed three times with methanol (50 ml). The washed powder was dried under vacuum at 40 °C for 12 h.

5.3.2 SYNTHESIS OF CADMIUM MYRISTATE – *VIA* CADMIUM TRIFLUOROACETATE FROM CADMIUM OXIDE

Cadmium myristate was synthesized starting from cadmium oxide according to the procedure described by Rossinelli *et al.*[25] In a 50 mL round bottom flask, cadmium oxide (44.8 mmol, 5.75 g, 1.0 eq.) was mixed with acetonitrile (20 mL) and cooled with a water-ice-bath. Trifluoroacetic acid (9.1 mmol, 0.7 mL, 0.2 eq) and trifluoroacetic anhydride (44.6 mmol, 6.2 mL, 1.0 eq) were slowly added. After 30 min stirring, a sludge formed, which was heated up to 60 °C and was stirred for additional 30 min until the solution turned colorless. To obtain the formed $Cd(TFA)_2$, the reaction mixture was cooled down and filtered. The colorless residue was washed with cold acetonitrile and dried under vacuum for 72 h. To obtained cadmium myristate, myristic acid (20.56 g; 90 mmol, 2.0 eq) and triethylamine (10.246 g, 101.3 mmol, 2.3 eq) were mixed in iso-propanol (180 mL). The cadmium trifluoroacetate solution was added dropwise to the myristic acid solution while stirring. The formed colorless precipitate was vacuum-filtered and was washed with cold methanol (3 times 50 mL). The final product was collected and dried under vacuum over night at 40 °C. To produce cadmium myristate with different amount of triethylamine, the precipitate was washed 4 times with 50 mL cooled methanol. After each washing step, a small amount of the precipitate was collected. The "magic" precursor was synthesized according to this procedure by a former lab member (Paul Kolpakov).

5.3.3 Synthesis of Cadmium Selenide Nanoplatelets

CdSe NPLs were synthesized following a modified procedure described by Rossinelli *et al.*[25] In a 100 ml three-neck flask cadmium myristate (0.282 mmol, 160 mg) and selenium powder (0.152 mmol, 12 mg) were added to 1-ocatadecene (15 mL). The mixture was degassed under vacuum and magnetic stirring at room temperature for 20 min. First, the temperature was increased to 110 °C in 10 min under argon atmosphere. After holding the temperature for 10 min at 110 °C under vacuum, the mixture was heated to 240 °C in 16 min under argon atmosphere. This temperature was kept constant for 8 min. During the temperature ramp to 240 °C, cadmium acetate dihydrate (0.347 mmol, 80 mg) was added when the temperature of the reaction mixture reached 188 °C (or 200 °C depending on the protocol, see main text). At the end of the temperature program, the reaction mixture was rapidly cooled with a water-bath. At 185 °C oleic acid (0.5 mL) was added. At 50 °C, hexane (5 mL) was added and a crude reaction product was collected.

During the synthesis, aliquots were taken for spectroscopic analyses. The first aliquots was collected 30s before the addition of $Cd(OAc)_2$, then every 30 sec after cadmium acetate dihydrate addition until the end of the temperature program. Afterward, 100 µL

aliquot solution, 150 µL oleic acid and 500 µL hexane were mixed and stirred for at least 3 h before measuring absorption and photoluminescence spectra.

For *in situ* absorption spectroscopy the reaction needed to be up-scaled four times. For *in situ* photoluminescence spectroscopy the reaction volume needed to be up-scaled two times.

Triethylamine as an impurity was tested, through a synthesis with the impure precursor (myristate:TEA ratio = 1:0.23) (see section 5.3.2) and by a synthesis with a ratio of myristate:TEA of 1:0.185, therefore pure cadmium myristate (0.055 mmol; 31.4 mg) was mixed with impure myristate (0.244 mmol; 138.6 mg; myristate:TEA = 1:0.23).

When trifluoroacetic acid was tested as impurity, the same reaction protocol as described above was applied and trifluoroacetic acid (5 µL or 10 µL) was added after the degassing step at 110°C under argon atmosphere.

When cadmium trifluoroacetate tested as impurity, a certain mol fraction of cadmium myristate (when Cd(TFA)$_2$ was added from the beginning) or cadmium acetate dihydrate (when Cd(TFA)$_2$ was added together with Cd(OAc)$_2$ was replaced with Cd(TFA)$_2$.In both cases the salts were mixed prior to addition. In table 3, the used amounts of cadmium salts are given.

TABLE 3:   In section 3.3.2.3 used amounts of cadmium trifluoroacetate.

Mol fraction / [mol%]	Cadmium trifluoroacetate		Cadmium myristate		Cadmium acetate dihydrate	
	m / [mg]	n / [mmol]	m / [mg]	n / [mmol]	m / [mg]	n / [mmol]
5	4.8	0.014	152.1	0.268	80.9	0.304
10	10.1	0.030	144.5	0.255	80.3	0.302
25	26.3	0.078	160.5	0.283	60.6	0.228
40	40.8	0.121	160.8	0.284	48.1	0.180
50	51.8	0.153	160.6	0.283	40.5	0.152
75	76.8	0.227	160.4	0.283	20.0	0.075
100	105.3	0.311	161.0	0.284	-	-

6 REFERENCES

[1]   W. E. Buhro, V. L. Colvin *Nat. Mater.* **2003**, *2*, pp. 138
        DOI: 10.1038/nmat844

[2]   G. H. V. Bertrand, *et al.*, *Chem. Commun.* **2016**, *52*, pp. 11975
        DOI: 10.1039/c6cc05705e

[3]   Y. Chen, *et al.*, *J. Am. Chem. Soc.* **2017**, *139*, pp. 10009–10019
        DOI: 10.1021/jacs.7b04855

[4]   A. Riedinger, *et al.*, *Nat. Mater.* **2017**, *16*, pp. 743–748
        DOI: 10.1038/nmat4889

[5]   S. Ithurria, *et al.*, *Nat. Mater.* **2011**, *10*, pp. 936-941
        DOI: 10.1038/nmat3145

[6]   V. I. Kilmov, *Los Alamos Science* **2003**, *28*, pp. 214-220

[7]   A. Efros, A.L. Efros, *et al. Sov. Phys. Semicond.* **1982**, *16* (7), pp. 772-775

[8]   V. K. LaMer, R. H. Dinegar, *J. Am. Chem. Soc.* **1950**, *72* (11), pp. 4847-4854
        DOI: 10.1021/ja01167a001

[9]   V. K. LaMer, *Ind. Eng. Chem.* **1952**, *44* (6), pp. 1270-1277
        DOI: 10.1021/ie50510a027

[10]   T. Sugimoto, *J. Colloid Interface Sci.* **2007**, *309*, pp. 106-118
        DOI: 10.1016/j.jcis.2007.01.036

[11]   N. T. K. Thanh, M. Maclean, S. Mahiddine, *Chem. Rev.* **2014**, *114*, pp. 7610–7630
        DOI: 10.1021/cr400544s

[12]   W. Ostwald, *Z. Phys. Chem.* **1900**, *34*, pp. 495-503
        DOI: 10.1515/zpch-1900-3431

[13]   M. Olutas, *et al.*, *ACS Nano* **2015**, *9*, pp. 5041–5050
        DOI: 10.1021/acsnano.5b01927

[14]   M. Nasilowski, *et al.*, *Chem. Rev.* **2016**, *116*, pp. 10934–10982
        DOI: 10.1021/acs.chemrev.6b00164

[15]   C. E. Rowland *et al.*, *Nat. Mater.* 2015, *14*, pp. 484–489
        DOI: 10.1038/nmat4231

[16]   C. She, *et al. Nano Lett.* **2014**, *14*, pp. 2772–2777
        DOI: 10.1021/nl500775p

[17]   A. Yeltik, *et al.*, *J. Phys. Chem. C* **2015**, *119* (47), pp. 26768–26775
        DOI: 10.1021/acs.jpcc.5b09275

[18]   A. Lyashchova, *et al.*, *Nanoscale Res. Lett.* **2014**, *9* (88)
        DOI: 10.1186/1556-276X-9-88

[19]   M. Ohara and R. C. Ried, "Modeling Crystal Growth Rates from Solution", *Prentice-Hall* **1973**

[20]   X. G. Peng, *et al.*, *Nature* **2000**, *404*, pp. 59–61
        DOI: 10.1038/35003535

[21]   M. R. Kim, *et al.*, *ACS Nano* **2012**, *6* (12), pp. 11088–11096
        DOI: 10.1021/nn3048846

[22]   S. Christodoulou, *et al.*, *Nano Lett.* **2018**, *18* (10), pp. 6248-6254
        DOI: 10.1021/acs.nanolett.8b02361

[23] W. Cho, *et al.*, *Chem. Mater.* **2018**, *30*, pp. 6957–6960
DOI: 10.1021/acs.chemmater.8b02489

[24] M. P. Hendricks, *et al.*, *science* **2015**, *348* (6240), pp. 1226-1230
DOI: 10.1126/science.aaa2951

[25] A. A. Rossinelli, *et al.*, *Chem. Commun.* **2017**, *53*, pp. 9938-9941
DOI: 10.1039/c7cc04503d

[26] C. Bullen, *et al.*, *Chem. Mater.* **2010**, *22* (14), pp. 4135–4143
DOI: 10.1021/cm903813r

[27] X. Cai, *et al.*, *J. Phys. Chem. C* **2013**, *117* (15), pp. 7902-7913
DOI: 10.1021/jp400688g

[28] Y. Zhao, *et al.* *ACS Nano* **2012**, *6* (10), pp. 9058-9067
DOI: 10.1021/nn303217q

[29] A. Y. Koposov, *et al.*, *J. Phys. Chem. C* **2018**, *122* (9), pp. 5119-5123
DOI: 10.1021/acs.jpcc.7b10615

[30] I. Fedin, D. V. Talapin *J. Am. Chem. Soc.* **2016**, *138* (31), pp. 9771–9774
DOI: 10.1021/jacs.6b05862

[31] F. D. Ott, *et al.*, *Nano Lett.* **2017**, *17* (11), pp. 6870-6877
DOI: 10.1021/acs.nanolett.7b03191

[32] S. Kudera, *et al.* *Adv. Mater.* **2007**, *19*, pp. 548-552
DOI: 10.1002/adma.200601015

[33] T. L. Marshbanks, *et al.*, *Thin Solid Films* **1993**, *232*, pp. 126-138
DOI: 10.1016/0040-6090(93)90774-J

[34] S. Tougaard, *Surf. Interface Anal.* **1997**, *25*, pp. 137-154
DOI: 10.1002/(SICI)1096-9918(199703)25:3<137::AID-SIA230>3.0.CO;2-L

[35] M. A. Mesubi, *J. Mol. Struct.* **1982**, *81*, pp. 61-71
DOI: 10.1016/0022-2860(82)80079-3

[36] N.W. Alcock, *et al.*, *J. Chem. Soc., Dalton Trans.* **1976**, *0*, pp. 2243-2246
DOI: 10.1039/DT9760002243

[37] Spectra Database for Organic Compounds SDBS, sodium myristate, IR: KBr disc
https://sdbs.db.aist.go.jp/sdbs/cgi-bin/landingpage?sdbsno=7379
https://sdbs.db.aist.go.jp/sdbs/cgi-bin/IMG.cgi?img-dir=ir&fname=NIDA21814&sdbsno=7379
(accessed march 31, 2019)

[38] Spectra Database for Organic Compounds SDBS, triethylamine, IR: liquid film
https://sdbs.db.aist.go.jp/sdbs/cgi-bin/landingpage?sdbsno=7379
https://sdbs.db.aist.go.jp/sdbs/cgi-bin/IMG.cgi?img-dir=ir&fname=NIDA678&sdbsno=1288
(accessed march 31, 2019)

[39] M. V. Kovalenko, *et al.*, *ACS Nano* **2015**, *9* (2), pp. 1012-1057
DOI: 10.1021/nn506223h

[40] Y. A. Yang, *et al.*, *Angew. Chem. Int. Ed.* **2005**, *44*, 6712-6715
DOI: 10.1002/anie.200502279

7 LIST OF FIGURES

8 LIST OF TABLES

ACKNOWLEDGMENTS